# Superior performance and resistance to $SO_2$ and $H_2O$ over $CoO_x$-modified $MnO_x$/biomass activated carbons for simultaneous $Hg^0$ and NO removal

Lei Gao[a,b], Caiting Li[a,b,*], Shanhong Li[a,b,*], Wei Zhang[c], Xueyu Du[a,b], Le Huang[a,b], Youcai Zhu[a,b], Yunbo Zhai[a,b], Guangming Zeng[a,b]

[a] College of Environmental Science and Engineering, Hunan University, Changsha 410082, PR China
[b] Key Laboratory of Environmental Biology and Pollution Control (Hunan University), Ministry of Education, Changsha 410082, PR China
[c] School of Energy and Power Engineering, Changsha University of Science & Technology, Changsha 410114, PR China

## HIGHLIGHTS

- 15%CoMn/BAC exhibited preferable performance for NO and $Hg^0$ simultaneous removal.
- 15%CoMn/BAC displayed excellent $SO_2$ and $H_2O$ resistance.
- The introduction of Co species into Mn/BAC could tremendously modify its physicochemical properties.
- The positive synergistic effect between $MnO_x$ and $CoO_x$ was achieved.
- The mutual effects of NO removal and $Hg^0$ removal were investigated.

## GRAPHICAL ABSTRACT
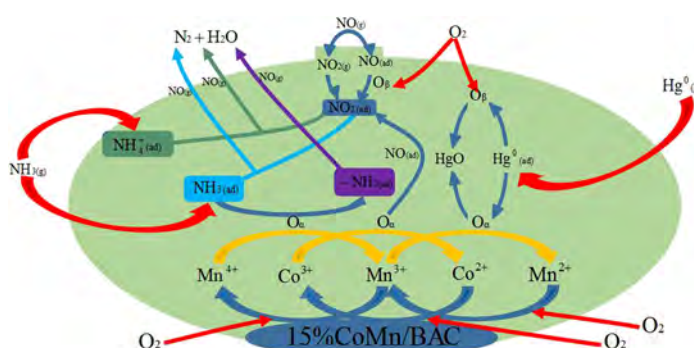


## ARTICLE INFO

## ABSTRACT

A series of $CoO_x$ modified $MnO_x$/biomass activated carbons (CoMn/BACs) prepared by the ultrasound-assisted impregnation method were employed for the simultaneous removal of NO and $Hg^0$ from simulated coal-fired flue gas for the first time. The physicochemical properties of such samples were characterized by XRD, BET, SEM, TEM, $NH_3$-TPD, $H_2$-TPR, FTIR, TG and XPS. 15%CoMn/BAC exhibited preferable performance for NO and $Hg^0$ removal in a wide temperature range from 160 to 280 °C, and it yielded prominent NO removal efficiency (86.5%) and superior $Hg^0$ removal efficiency (98.5%) at 240 °C. The interaction between NO removal and $Hg^0$ removal lessened corresponding separate efficiency, the adverse effect of $NH_3$ on $Hg^0$ removal could not be offset by promotional influences of NO and $O_2$. Compared with 15%Mn/BAC, the addition of $CoO_x$ with suitable amount into 15%CoMn/BAC could contribute to the synergistic effect between $MnO_x$ and $CoO_x$, resulting in the increase of BET surface area and surface active oxygen species as well as $Mn^{4+}$ concentration, the enhancement of redox ability and the strength or amount of surface acid sites, restraining the crystallization of $MnO_x$, which might be responsible for the improvement of catalytic performance and resistance to $SO_2$ and $H_2O$. Additionally, the hydrophobic property of BAC further strengthened $H_2O$ tolerance. The results of stability and recyclability tests indicated that 15%CoMn/BAC possessed a promising application potential for NO and $Hg^0$ simultaneous removal at low temperature.

* Corresponding authors at: College of Environmental Science and Engineering, Hunan University, Changsha 410082, PR China.
  *E-mail addresses:* ctli@hnu.edu.cn (C. Li), lsh-17208@hnu.edu.cn (S. Li).

## 1. Introduction

NO and $Hg^0$ emissions emitted from coal combustion have triggered tremendous attention worldwide due to their marked quantities and adverse effects on the environment and human health [1–5]. To respond to these increasing environmental awareness and rigorous emission regulations and standards, a wealth of technologies for separately lessening NO and $Hg^0$ emissions have been developed [2,6,7]. Among which, selective catalytic reduction with $NH_3$ ($NH_3$-SCR) has long been the predominant mature technology for NO abatement due to its acceptable cost, satisfactory reliability and efficiency, where $V_2O_5$-$WO_3(MoO_3)/TiO_2$ is the commonly utilized commercial catalyst [8]. Nevertheless, vanadium-based SCR catalyst suffers from some non-negligible shortages such as biological toxicity and volatility of vanadium species, the over-oxidation of $NH_3$, the narrow active temperature range of 300–400 °C, and the infaust conversion of $SO_2$–$SO_3$ [9]. Moreover, the narrow active temperature window of aforesaid catalyst urges the SCR system to be installed upstream of the desulfurization unit and dust remover device where catalysts are susceptible to $SO_2$ and dust [10]. It is well-known that mercury exists in three forms in coal combustion flue gas. Thereinto, oxidized mercury ($Hg^{2+}$) and particle-bound mercury ($Hg^P$) can be easily captured by the existing wet flue gas desulfurization (WFGD) and electrostatic precipitator (ESP) or fabric filter (FF) systems, while $Hg^0$ emission is relatively untoward to be alleviated by existing environmental protection apparatuses owing to its insolubility in water and high volatility [11]. By far, activated carbon injection (ACI) is the commercially commonly adopted technology for controlling $Hg^0$ emission [2,12]. However, some inevitable shortcomings are related with the ACI technology, which consists of low adsorption efficiency at high temperature, slow regeneration rates, huge operating costs, the value decline of reclaimed fly ash, and potential secondary contamination caused by spent ACs [5,12,13]. Furthermore, nowadays the respective control $Hg^0$ and NO technology is widely adopted in coal-fired power plants, confronting several intractable bottlenecks such as huge land requirement, large equipment investment, high operating and maintaining costs [2,5].

It is recognized that vanadium-based SCR catalyst not only exhibits outstanding denitration efficiency but also shows the co-benefit for boosting the oxidation of part $Hg^0$ to HgO, which can be removed through subsequent WFGD [1,12]. In addition, relevant statistics manifested that with 2-year operating time and 55% Hg removal efficiency, the cost through catalytic oxidation technology was only 60% of that though ACI technology [14]. Therefore, compared two $Hg^0$ removal strategies, catalytic oxidation outperformed ACI in the aspects of decent durability, relatively low cost, no additional equipment, indicating broad application prospects. However, the conversion from $Hg^0$ to HgO in low chlorine flue gas was not effective enough by widely engaged $V_2O_5$-$WO_3(MoO_3)/TiO_2$ catalyst [3,13]. Fortunately, that provides us a direction for designing novel vanadium-free and low-temperature catalysts with splendid denitration and demercuration efficiencies, which can realize the integration of NO and $Hg^0$ abatement by the existing devices, overcoming the above-mentioned deficiencies. Thus such catalyst can not only save the land occupation, equipment investment and operating cost of mercury removal, but also make the SCR unit be placed downstream of desulfurization unit and dust remover device, thus reducing the energy consumption for heating the flue gas and alleviating catalyst deactivation from $SO_2$ and dust. Consequently, it is of great significance and urgency to develop efficient catalysts for NO and $Hg^0$ simultaneous removal at low temperature.

Recently, a battery of catalysts, such as $V_2O_5$-$CeO_2/TiO_2$, $TiCe_{0.25}Sn_{0.25}O_x$, Mn-Ce/MOFs, $MnO_x/Co_{0.3}Ce_{0.35}Zr_{0.35}O_2$, $CuCl_2$-$CoO_x/TiCe$, $TiAl_{10}Ce_{20}$, have been developed for simultaneous removal of NO and $Hg^0$ [12,15–19]. Particularly, manganese oxides ($MnO_x$) with preeminent low temperature performance have been a research focus for NO or $Hg^0$ removal owing to high oxygen storage/release capacity, the nature of labile oxygen, diversiform oxidation states and

outstanding redox properties as well as abundant reserves, cheap price and environmental friendliness of Mn species [6,9,20,21]. It was envisaged that $Mn^{4+}$ was the most active species and the valence change from $Mn^{4+}$ to $Mn^{3+}$ and therewith to $Mn^{2+}$ in Mn-based catalysts was the possible mechanism for both $Hg^0$ oxidation and NO reduction, in which the multiple valences and large-span valence change of Mn species should be responsible for perfect low temperature request [3,7,21,22]. Nevertheless, poor resistance to $SO_2$ and $H_2O$, low specific surface area and thermal instability remained intractable challenges for some $MnO_x$-based catalysts especially unsupported $MnO_x$ catalysts, impeding their actual applications [9,13]. Zhang et al. discovered that both NO and $Hg^0$ removal efficiencies over $MnO_x/TiO_2$ catalysts were remarkably suppressed by $SO_2$, and $Hg^0$ removal efficiency sharply decreased from 63.4% to even 5% after adding 400 ppm $SO_2$ [13,23,24]. Therefore, it is imperative to improve $SO_2$ and $H_2O$ resistance of such Mn-based catalysts before they can be widely adopted as commercial catalysts for NO and $Hg^0$ simultaneous removal.

Likewise, Co-based catalysts have obtained a great deal of interests in catalysis due to unique redox properties, advantageous morphology characteristics and high bulk oxygen species, and they can exhibit good activity for NO reduction, VOCs and $Hg^0$ oxidation [11,25–27]. Additionally, previous works reported that the addition of Co oxides into Mn species could dramatically improve NO and VOC removal efficiencies compared with those of single Mn and Co oxides, which was attributed to the enhancement of active oxygen species and redox property derived from the strong interaction of Mn and Co species [11,26,27]. Thus, it was sensible to deduce that Co-modified Mn-based catalysts might show satisfactory performance for NO and $Hg^0$ simultaneous removal. Even so, few reports have concentrated on simultaneously removing NO and $Hg^0$ over such catalysts, including the tolerance to $SO_2$ and $H_2O$ in that processes [13]. What's more, the negative effect of $H_2O$ on low temperature catalytic activity over such catalysts was usually neglected [4]. On the contrary, we discovered that carbon-based catalysts with carriers like AC and BAC often exhibited good $H_2O$ resistance in our previous works [2,5], which might be due to the hydrophobic property of carbon materials [28,29]. To the best of our understanding, $CoO_x$ modified $MnO_x/BAC$ for $Hg^0$ and NO simultaneous removal has not been related to in literature, in which the synergistic effect between $CoO_x$ and $MnO_x$ might contribute to the enhancement of catalytic performance and resistance to $SO_2$ and $H_2O$. Therefore, a series of tests are conducted to investigate the role of $CoO_x$ in CoMn/BAC catalysts on the performance and resistance to $SO_2$ and $H_2O$ for $Hg^0$ and NO simultaneous removal in this work.

## 2. Materials and methods

### 2.1. Sample preparation

Agricultural straws were gathered from the countryside area of Xinyang city, Henan Province, PR China. The preparation methods of BAC carrier were described in detail in our previous work [2]. The catalysts were prepared by ultrasound-assisted impregnation method adopting manganese acetate or cobalt nitrate as the precursors of active ingredients. The first step was to measure the water adsorption capacity of BAC carrier. Second, desired amounts of manganese acetate or cobalt nitrate were added into moderate deionized water to form completely dissolved solutions. Third, calculated amounts of BACs were impregnated in aforementioned solutions for 24 h, including ultrasound treatment of 1 h. Therewith, the impregnated samples were placed in a drying oven of 105 °C until completely dry and calcined at 500 °C for 4 h in a tube furnace with $N_2$ atmosphere. The atomic ratio of Co/Mn was 1:2 in all CoMn/BAC samples, which was selected due to its preferable performance in our preliminary experiments. Thus, modified BAC catalysts were denoted as XCoMn/BAC, where X was ascribed to the mass percentage of CoMn complex oxides, which was respectively assigned a value of 7.5%, 15%, 22.5% and 30% in this work.

Meanwhile, XCo/BAC and XMn/BAC as well as virgin BAC were prepared by the similar method for comparison.

### 2.2. Sample characterization

The textural characteristics of samples were measured using $N_2$ adsorption/desorption at $-196\,°C$ by an automatic Micromeritics ASAP2460 volumetric sorption analyzer (Micromeritics Instrument Corp., USA). Before formal test, each sample was degassed at $120\,°C$ for 3 h in a flow of $N_2$. The pore size distributions and specific surface areas were determined by Barrett-Joyner-Halenda (BJH) and Brunauer-Emmett-Teller (BET) method, respectively. Thus, the results of average pore diameters, total pore volumes and specific surface areas were acquired.

Samples' scanning electron microscopy (SEM) photographs were taken by the Hitachi S-4800 analyzer (Hitachi Limited, Japan) to analyze their surface structure and morphology. Transmission Electron Microscope (TEM) images were carried out on the Tecnai G2 F20 (FEI, USA) to further observe their microstructures.

The component dispersivity and crystallinity of the samples were collected on a Bruker D8-Advance X-ray diffraction device, which was equipped with Cu Ka radiation ($\lambda = 1.543\,Å$, 40 kV, 40 mA).

Ammonia-temperature programmed desorption ($NH_3$-TPD) and $H_2$-temperature programmed reduction ($H_2$-TPR) were performed using the TP-5080 automatic chemical adsorption instrument (Tianjin Xianquan, China).

The element chemical state and chemical composition of virgin BAC, fresh 15%Mn/BAC, fresh and used 15%CoMn/BAC were investigated by a K-Alpha 1063 X-ray photoelectron spectrometer (Thermo Fisher Scientific, USA) using Al Ka radiation of 72 W.

The surface adsorbed species of 15%CoMn/BAC after different reactant molecules adsorption were detected by FTIR experiments using a FTIR IRInfinity-1 spectrometer. Prior to formal test, the sample was pretreated under $N_2$ for 2 h to wipe off possible adsorbed species at $260\,°C$. Whereafter, corresponding adsorption tests were carried out for 1 h at ambient temperature.

Thermogravimetric (TG) analysis was carried out with a DTG-60 thermal analyzer (Shimadzu, Japan) in a $N_2$ atmosphere with a heating rate of $10\,°C/min$ to investigate the thermal stability of fresh and used 15%CoMn/BAC and 15%Mn/BAC.

### 2.3. Experimental setup and procedure

The experimental apparatus diagram for NO and $Hg^0$ simultaneous removal was shown in Fig. 1. The simulated flue gas (SFG) with a total flow of 500 mL/min was composed of 500 ppm NO, 500 ppm $NH_3$, $100\,μg/m^3$ $Hg^0(g)$, 6% $O_2$, and $N_2$ as the balance gas. Other gas compositions were supplied when needed. NO, $NH_3$, $SO_2$, $N_2$ and $O_2$ were from corresponding cylinders and accurately controlled by matched mass flow controllers. Before entering the reactor, these gases intermingled with each other in a gas mixing equipment. Prior to formal test, the blank test of the experiment system was carried out to inspect the effects of the reactor and pipes on NO and $Hg^0$ removal until the system became steady and their effects were negligible. In each test, 200 mg sample corresponded to a space velocity of about $180,000\,h^{-1}$ was placed in the central part of the fixed bed reactor which was composed of a quartz tube (10 mm inner diameter × 600 mm length) and a digital temperature controller. In order to distinguish the outlet mercury speciation, a mercury conversion test was performed, as described in our previous works [2,5]. In which the outlet flue gas from the reactor had two freely switching branches, one got through 10% KCl aqueous solution to eliminate $Hg^{2+}$ for remanent $Hg^0$ measurement, while the other passed 10% $SnCl_2$ + HCl aqueous solution to reduce $Hg^{2+}$ to $Hg^0$ for gauging total mercury ($Hg_{out}^{0\,T}$). The MGA 5 flue gas analyzer (Germany) and Lumex RA-915 M mercury analyzer (Russia) with detection limit of $2\,ng/m^3$ were employed to respectively measure the

inlet and outlet concentrations of NO and $Hg^0$. The performances of samples on $Hg^0$ and NO simultaneous removal were evaluated by $Hg^0$ removal efficiency ($E_{Hg}$) and NO removal efficiency ($E_{NO}$), which were calculated by Eqs. (1) and (2), respectively. Similarly, the oxidation efficiency of $Hg^0$ ($E_{oxi}$) was determined by Eq. (3).

$$E_{Hg} = \frac{Hg_{in}^0 - Hg_{out}^0}{Hg_{in}^0} \times 100\% \tag{1}$$

$$E_{NO} = \frac{NO_{in} - NO_{out}}{NO_{in}} \times 100\% \tag{2}$$

$$E_{oxi} = \frac{Hg_{out}^0\,T - Hg_{out}^0}{Hg_{in}^0} \times 100\% \tag{3}$$

In which $Hg_{in}^0$ and $Hg_{out}^0$ represented the inlet and outlet $Hg^0$ concentration, respectively. Similarly, the inlet and outlet NO concentration were respectively denoted by $NO_{in}$ and $NO_{out}$. In addition, to lessen the experimental errors, $E_{Hg}$ and $E_{NO}$ were the average of two or three group data of parallel tests and the relative errors were limited to less than 5%.

## 3. Results and discussion

### 3.1. Characterization of samples

#### 3.1.1. BET analysis

The $N_2$ adsorption/desorption isotherms and corresponding pore size distribution curves of virgin BAC and modified BACs were depicted in Fig. 2A and B, respectively. All these isotherms were assigned to the type IV with H3 hysteresis loops, indicating the presence of slit shaped mesopores [30,31]. The pore size distribution curves all presented narrow unimodal peaks centered at 2.4 nm, suggesting that both mesopores and micropores coexisted in these samples [31,32]. In addition, the textural parameters such as BET surface area, total pore volume and average pore diameter of these samples were collected in Table 1. It could be clearly observed that virgin BAC held bigger surface area ($745.935\,m^2/g$) and total pore volume ($0.485\,cm^3/g$) than those of modified BACs. The BET surface area, total pore volume and average pore diameter of modified BACs decreased with the increase of loading value of metal oxides. Thereinto, 30%CoMn/BAC owned the smallest BET surface area of $489.42\,m^2/g$, the poorest total pore volume of $0.31\,cm^3/g$ and the narrowest average pore diameter of 2.53 nm. That appearance could be explained by that the pores would be deposited by metal oxides, and agglomerated metal oxides augmented with the enhancement of loading value, thus resulting in more and more of slit-like pores covered by Co and Mn species [2,5,30]. That was in well agreement with SEM and XRD results. Moreover, it was worth to note that 15%CoMn/BAC exhibited bigger BET surface area and total pore volume than those of 15%Mn/BAC and 15%Co/BAC, which might be attributed to the strong interaction between two metal oxides, in which the addition of Co species into Mn/BAC could promote metal oxides dispersion and inhibit their agglomeration [33,34].

#### 3.1.2. SEM and TEM analysis

The SEM images of virgin BAC and 7.5%-30%CoMn/BACs were presented in Fig. 3. The dark smoothness zones belonged to carbon enriched areas, while light zones denoted the existence of metal oxides. It was clearly seen that the pristine surface property of virgin BAC had suffered from substantial changes due to the introduction of metal oxides. As shown in Fig. 3B, metal oxides exhibited high dispersion and only a few agglomerates were observed, however, ubiquitous dark areas demonstrated the surface of 7.5%CoMn/BAC were not be fully utilized, where could be covered by additional metal oxides. It was widely recognized that more dispersed active metal oxides were propitious to better catalytic activity [2,5]. With regard to 15%CoMn/BAC, most surface areas of which were highly scattered by metal oxides and some agglomerates appeared, whereas serious agglomerates emerged on the
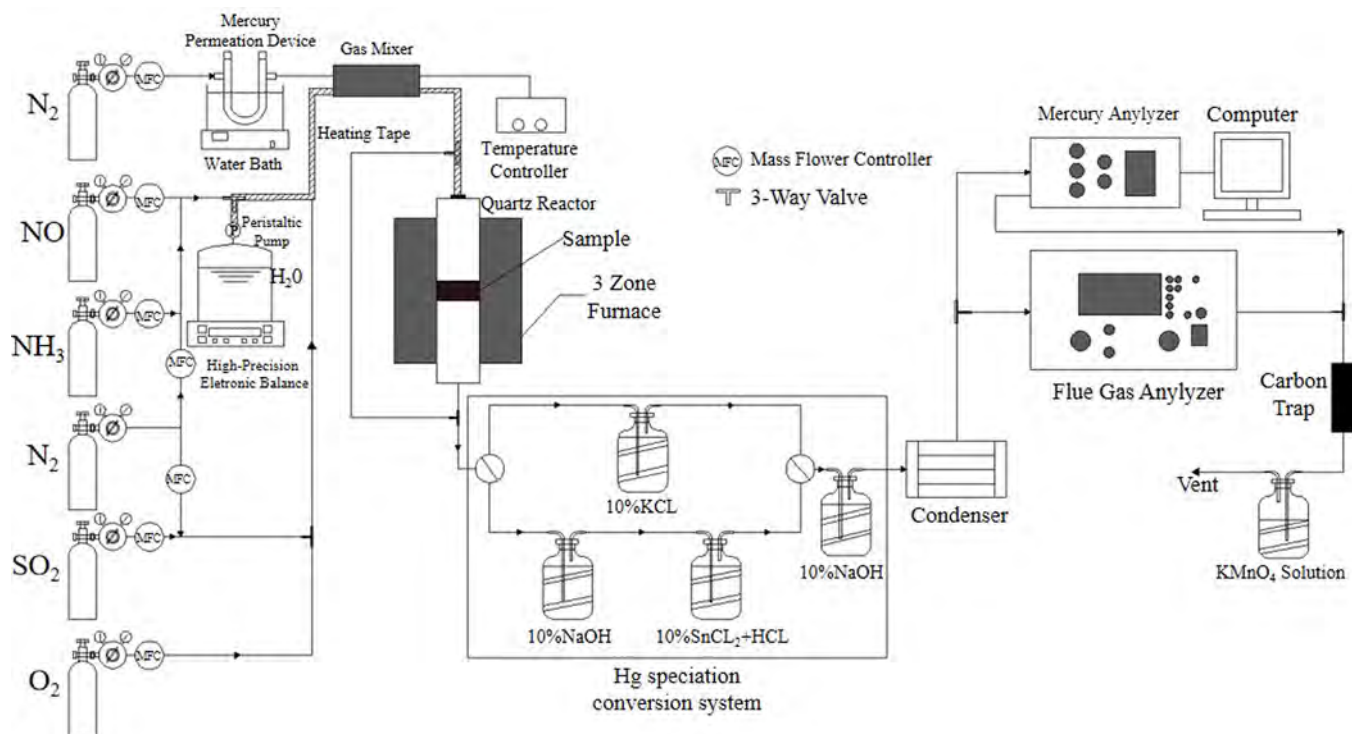
**Fig. 1.** The experimental apparatus diagram for NO and Hg$^0$ simultaneous removal.

surfaces of 22.5%CoMn/BAC and 30%CoMn/BAC. Thus, metal oxide agglomerates became bigger with the increase of metal oxides loading, resulting in the destruction of many preexisting pores and the decline of available catalytic active sites, which had a detrimental impact on both catalytic activity and the economy. This appearance was in good agreement with BET results.

Fig. 3 also displayed the TEM photographs of 15%Mn/BAC, 15%Co/BAC and 15%CoMn/BAC, in which crystalline nanoparticles with visible lattice fringes were observed. As shown in Fig. 3F, the primary particle size of 15%Mn/BAC was around 20 nm and three kinds of lattice fringes of 0.2545 nm, 0.2460 nm and 0.4876 nm were detected, which were ascribed to Mn$_3$O$_4$ (3 1 1) phase, MnO (0 2 1) phase and MnO$_2$ (1 1 1) phase, respectively. With regard to 15%Co/BAC, the primary particle size was around 17 nm and two kinds of lattice fringes

**Table 1**
The BET specific surface area and pore parameters of virgin BAC and modified BACs.

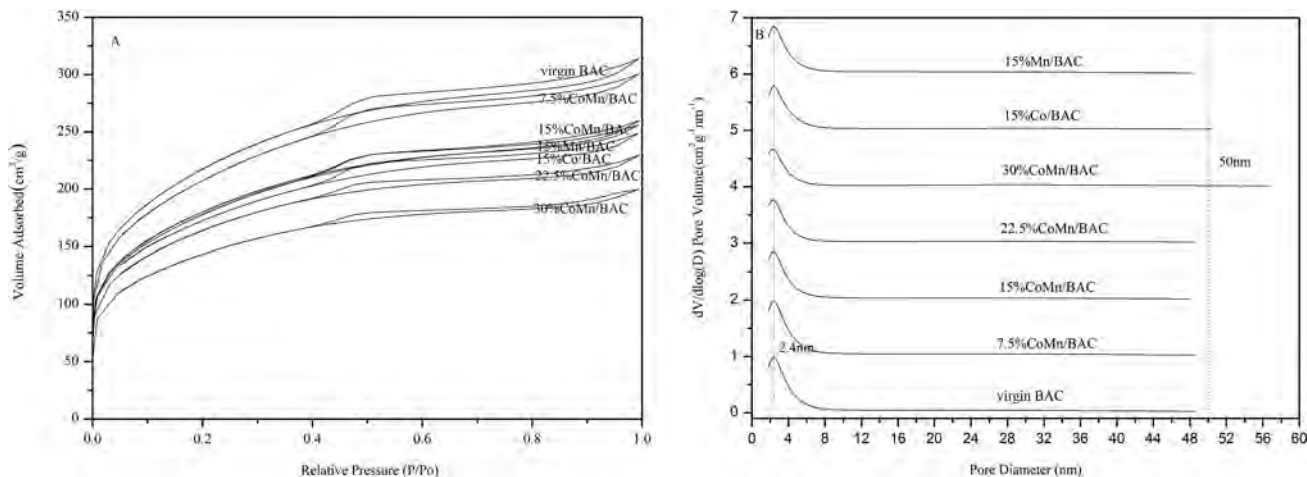| Sample | BET surface area (m$^2$/g) | Total pore volume (cm$^3$/g) | Average pore diameter (nm) |
|---|---|---|---|
| Virgin BAC | 745.935 | 0.485 | 2.603 |
| 7.5%CoMn/BAC | 712.017 | 0.465 | 2.612 |
| 15%CoMn/BAC | 617.149 | 0.402 | 2.568 |
| 22.5%CoMn/BAC | 560.356 | 0.356 | 2.539 |
| 30%CoMn/BAC | 489.420 | 0.310 | 2.530 |
| 15%Co/BAC | 590.756 | 0.385 | 2.605 |
| 15%Mn/BAC | 600.447 | 0.392 | 2.634 |



**Fig. 2.** The N$_2$ adsorption/desorption isotherms and corresponding pore size distribution curves of virgin BAC and modified BACs: (A) the N$_2$ adsorption/desorption isotherms, (B) the pore size distribution curves.
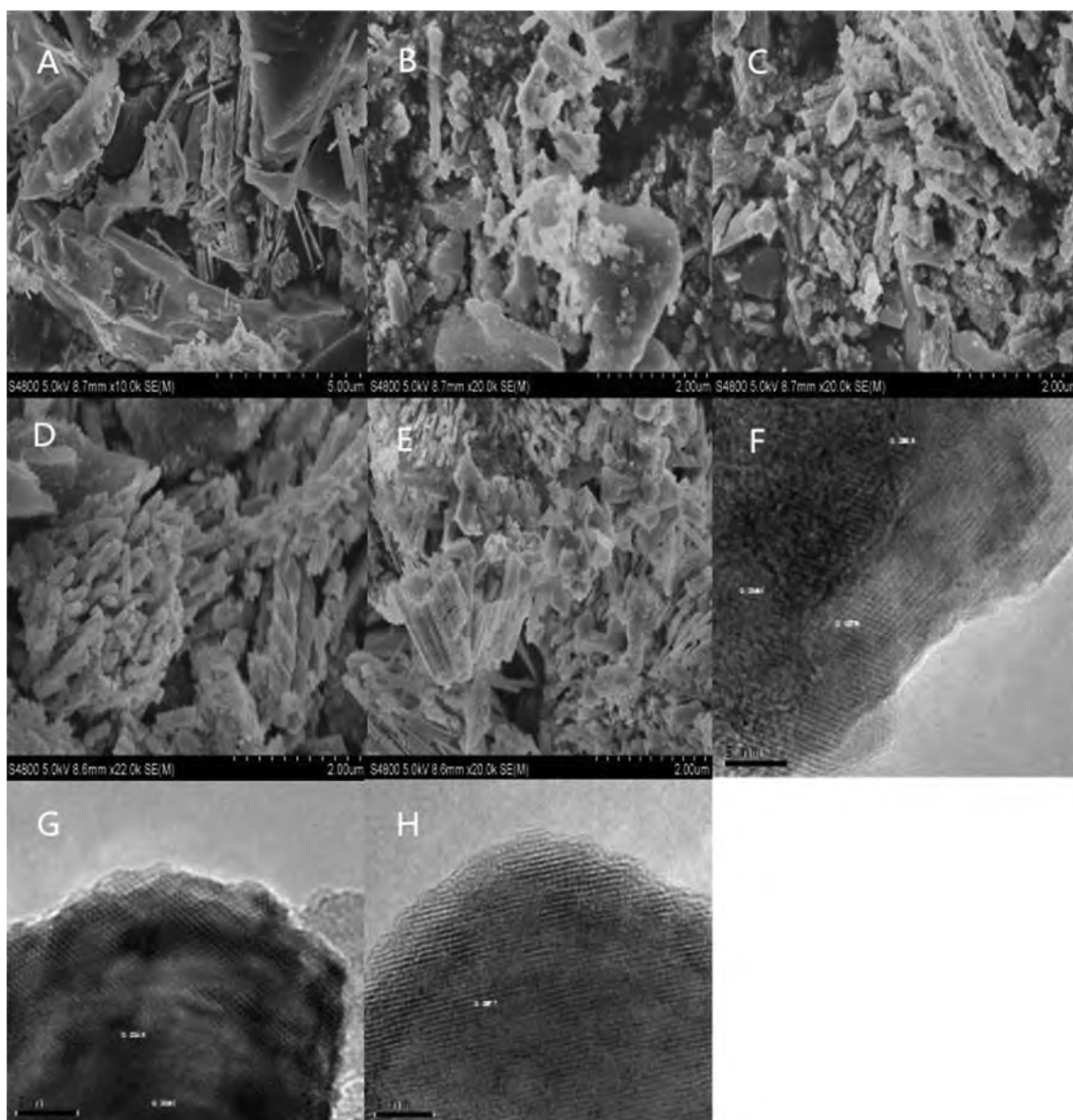
**Fig. 3.** The SEM and TEM images of virgin BAC and modified BACs. SEM: (A) virgin BAC, (B) 7.5%CoMn/BAC, (C) 15%CoMn/BAC, (D) 22.5%CoMn/BAC, (E) 30%CoMn/BAC, A × 10,000 multipulter; B, C, D and E × 20,000 multipulter; TEM: (F) 15%Mn/BAC, (G) 15%Co/BAC, (H) 15%CoMn/BAC.

of 0.2450 nm and 0.2145 nm were observed, which were assigned to $Co_3O_4$ (3 1 1) phase and CoO (2 0 0) phase, respectively [27]. For 15%CoMn/BAC, the primary particle size was about 14 nm and much smaller than that of 15%Mn/BAC and 15%Co/BAC, indicating that Co incorporation could somewhat lessen the particle size of 15Mn/BAC and alleviate its crystallinity. Only two kinds of lattice fringes of 0.2577 nm and 0.4541 nm corresponding to $CoMnO_3$ (1 0 4) and (0 0 3) phase were observed on 15%CoMn/BAC [35]. In addition, there was no lattice fringes matched $Mn_3O_4$, MnO, $MnO_2$, $Co_3O_4$ and CoO. This results indicated that Mn and Co species were well dispersed in the 15%CoMn/BAC or they existed as amorphous species.

### 3.1.3. XRD analysis

The XRD patterns of virgin BAC and modified BACs were depicted in Fig. 4. As for virgin BAC, four distinct diffraction peaks at 26.60°, 28.90°, 36.04° and 44.46° were detected, thereinto the peaks at 28.90° and 36.04° (PDF-ICDD 18-1170) were attributed to $SiO_2$ [36], whereas other ones at 26.60° and 44.46° (JCPDS 25-0284) were associated with the carbon matrix of BAC carrier [2]. Interestingly, they all decreased or even disappeared with the introduction of $MnO_x$ or $CoO_x$, and this
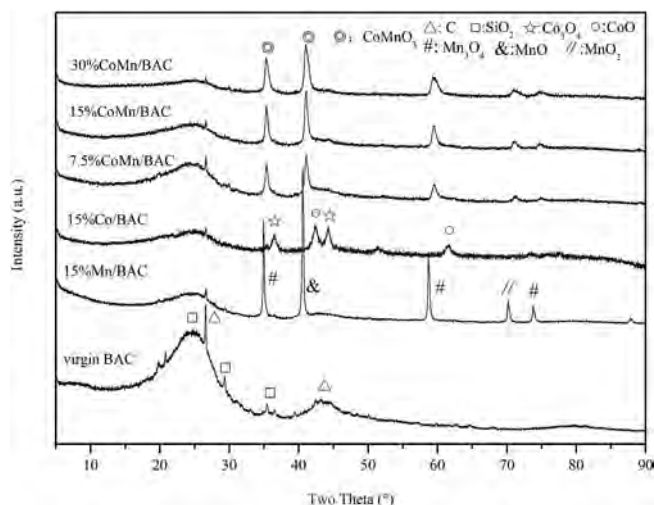


**Fig. 4.** XRD patterns of virgin BAC and modified BACs.

phenomenon became more and more apparent with the increase of metal oxides loading, indicating the pristine structure of virgin BAC had been significantly changed due to the loading of metal oxides and an intense interaction appeared among these metal oxides and BAC [2,36]. With regard to 15%Mn/BAC, five emerging peaks at $2\theta = 36.09°$, 40.55°, 59.84°, 69.5° and 73.8° were discovered. Meanwhile, the peaks at 36.09°, 59.84° and 73.8° (JCPDS 75-1560) were attributed to $Mn_3O_4$, the peak at 40.55° (JCPDS 72-1533) was assigned to MnO, and the peak at 69.5° (JCPDS 29-1020) represented the presence of $MnO_2$ [36,37]. As for 15%Co/BAC, four emerging peaks centered at $2\theta = 36.93°$, 42.39°, 44.85° and 61.49° were observed, in which the peaks at 36.93° and 44.85° (JCPDS 74-1656) corresponded to $Co_3O_4$ crystallites [38], while the other peaks at 42.39° and 61.49° (JCPDS 48-1719) were ascribed to CoO [2]. This phenomena demonstrated the coexistence of different Mn or Co species in these samples with perfect crystalline structure due to clear diffraction peaks, which were in good accordance with the results of $H_2$-TPR and XPS. Compared with 15%Mn/BAC and 15%Co/BAC, XCoMn/BACs displayed several emerging characteristic peaks at 36.4° and 41.6°, which were related to $CoMnO_3$ phase (JCPDS 12-0476), indicating that the dissolution of Co ions into $MnO_x$ lattice to form Mn-O-Co binary oxides, considering that the radius of $Co^{3+}$ (0.65 Å) and $Co^{2+}$ (0.78 Å) were closed to those of $Mn^{4+}$ (0.60 Å) and $Mn^{3+}$ (0.66 Å) [39,40]. No other diffraction peaks assignable to Co species were detected in XCoMn/BAC samples, which might be ascribed to its ultralow loading value and good dispersion [2,36]. Moreover, the presence of Co species might enhance the dispersion of Mn species by inhibiting agglomeration effect [33]. Additionally, other peaks belonged to Mn species weakened and broadened or even vanished in XCoMn/BAC samples, revealing that the introduction of Co species leaded to smaller size of Mn species in poorly crystalline state or amorphous surface species [33,39,41,42]. These Mn species in poor crystalline structure were anticipated to enhance catalytic performance due to facilitating surface oxygen vacancies [41,42].

### 3.1.4. $H_2$-TPR analysis

The redox abilities of virgin BAC and modified BACs were investigated by $H_2$-TPR, and the results were illustrated in Fig. 5. With regard to virgin BAC, the only reduction peak centered at 690 °C could be associated with the gasification of BAC bulk material [43], which was also observed in all modified BACs. The reduction of 15%Mn/BAC was related to three steps. The first peak located at 320 °C might be attributed to the reduction of $MnO_2–Mn_2O_3$, whereas the second peak appeared at 427.8 °C was probably due to the reduction of $Mn_2O_3–Mn_3O_4$. The third peak at 510 °C could correspond to
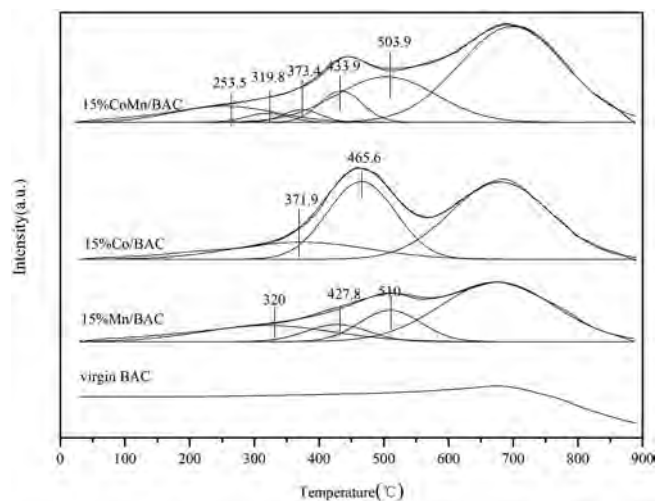
subsequent reduction of $Mn_3O_4–MnO$ [38,40]. As for 15%Co/BAC, two reduction peaks located at 371.9 and 465.6 °C were found, and the lower temperature peak was ascribed to the reduction of $Co^{3+}–Co^{2+}$ with concomitant structure change, while the higher temperature peak was associated with the stepwise reduction of CoO to metallic cobalt [40,44]. It was noted that 15%CoMn/BAC exhibited five peaks emerged at 253.5, 319.8, 373.4, 433.9 and 503.9 °C, in which the reduction profiles could be classified into two groups: the peaks centered at 253.5, 373.4 and 503.9 °C for $MnO_x$ and the other peaks at 319.8 and 433.9 °C for $CoO_x$. It was clearly seen that the reduction peaks of 15%CoMn/BAC shifted to lower temperatures, indicating it yielded better redox ability than those of 15%Mn/BAC and 15%Co/BAC [26,42]. That could be attributed to that the couples of $Mn^{4+}/Mn^{3+}$ and $Co^{3+}/Co^{2+}$ facilitated each other to decrease the energy demanded for the electronic transfer or the formation of more surface oxygen vacancies, thus significantly boosting oxygen mobility enhancement or reactants activation [30,42]. This also suggested that a synergistic effect emerged between $MnO_x$ and $CoO_x$, which might possibly contribute to surface oxygen defects and structural distortion, which were favorable for catalytic reactions [2,33,45]. Thus, that could be used to explain why 15%CoMn/BAC exhibited perfect catalytic activity at lower temperature range.

### 3.1.5. $NH_3$-TPD analysis

During $NH_3$-SCR of NO process, the surface acidity properties of catalysts were of vital importance for $NH_3$ adsorption and succedent activation. Therefore, we estimated the acidity properties of virgin BAC, 15%Mn/BAC, 15%Co/BAC and 15%CoMn/BAC by $NH_3$-TPD tests. As displayed in Fig. 6, only one small peak was observed about virgin BAC, revealing that it only owned a certain amount of acid sites. After loading Mn or Co metal oxides, it was clearly seen that two bigger and broader desorption peaks were detected in modified BACs, indicating the strength and amount of acid sites were immensely aggrandized after introducing metal oxides. Meanwhile, low temperature peaks were ascribed to Brønsted acid sites, while higher peaks were assigned to Lewis acid sites [46,47]. It was speculated that Brønsted acid sites were derived from surface hydroxyl groups [46,48], whereas Lewis acid sites might be associated with unsaturated $Mn^{n+}$ or $Co^{n+}$ sites [46,49]. The peak intensities and corresponding areas of 15%CoMn/BAC were much bigger than those of 15%Mn/BAC and 15%Co/BAC, and the synergistic effect between Mn and Co metal oxides might be responsible for more acid sites, which was beneficial for SCR activity because more acid sites meant more adsorbed and activated $NH_3$ [49]. It was reported that the presence of $Co^{3+}$ might contribute to the improvement of total acidity

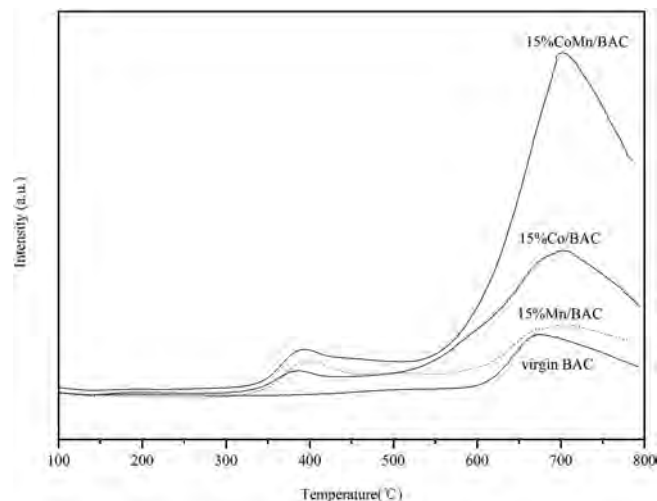**Fig. 5.** $H_2$-TPR curves of virgin BAC, 15%Mn/BAC, 15%Co/BAC and 15%CoMn/BAC.

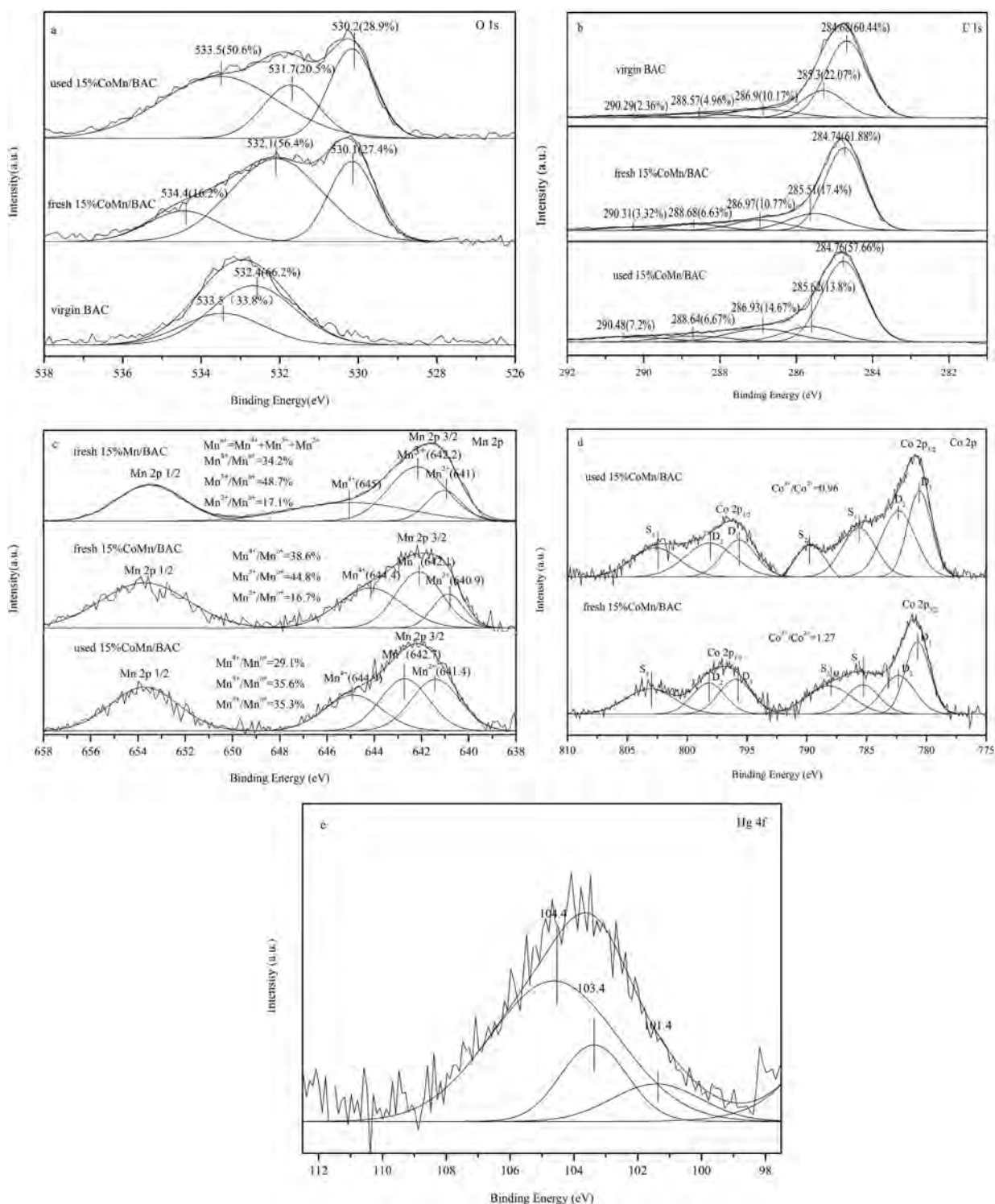**Fig. 6.** $NH_3$-TPD curves of virgin BAC, 15%Mn/BAC, 15%Co/BAC and 15%CoMn/BAC.

Fig. 7. XPS spectra of virgin BAC, fresh 15%Mn/BAC, fresh and used 15%CoMn/BAC: (a) O 1s, (b) C 1s, (c) Mn 2p, (d) Co 2p and (e) Hg 4f.

of a given catalyst owing to its high tendency for forming amino complexes [49,50].

### 3.1.6. XPS analysis

The element chemical state and composition of virgin BAC, 15% Mn/BAC, fresh and used 15%CoMn/BAC were elucidated by XPS, and the XPS spectra of O 1s, C 1s, Mn 2p, Co 2p and Hg 4f were presented in Fig. 7. In general, the O 1s XPS profile was composed of three type symmetrical peaks located at 530.1–530.2, 531.7–532.4 and 533.5–534.4 eV in these samples. The lower binding energy peak was related to lattice oxygen ($O_\alpha$); the medium one corresponded to chemisorbed oxygen, oxygen vacancies or weakly bonded oxygen ($O_\beta$); the higher one was ascribed to adsorbed water species ($O_\gamma$) [34,51,52]. Compared with fresh and used 15%CoMn/BAC, virgin BAC seemed short of $O_\alpha$, which could act as oxygen storage role and made surface oxygen more labile, thus boosting low-temperature catalytic activity [34]. In other words, the introduction of metal oxides could not only contribute to $O_\alpha$, but also promote catalytic activity. $O_\beta$ might derive
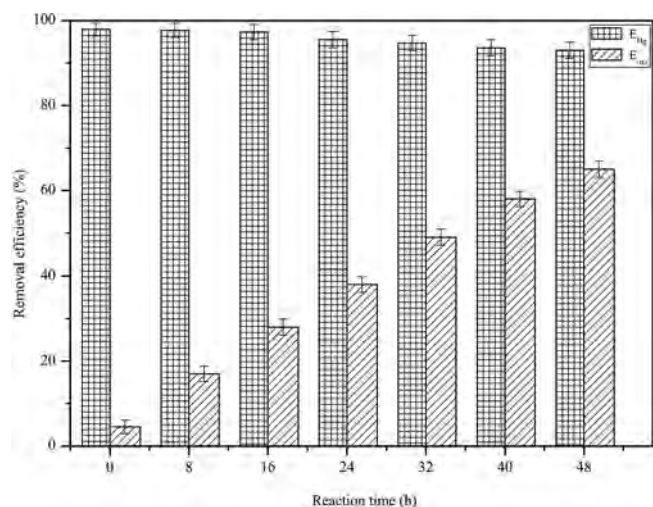
**Fig. 8.** The results of mercury conversion tests. Reaction conditions: T = 240 °C, 6% $O_2$, 100 μg/m³ $Hg^0$, 500 ppm NO, 500 ppm $NH_3$, $N_2$ as balance.

from oxygen-containing function groups of carriers and the transformation from fractional lattice oxygen [53,54]. It was worth mentioning that $O_β$ was deemed to be highly reactive in redox reactions due to better mobility and higher activity [2,42]. It was clearly seen that the ratio of $O_β$ descended markedly from 56.4% to 20.5% after reactions, on the contrary, $O_γ$ demonstrated obviously ascendant trend from 16.2% to 50.6%, while the ratio of $O_α$ increased slightly from 27.4% to 28.9%. That indicated that $O_β$ had participated in the reactions and been consumed in the phases. Particularly, previous works also confirmed $O_α$ to take part in these reactions [2,5].

As shown in Fig. 7b, the C 1s spectra fitting had been resolved into five component peaks located at 284.68–284.76 eV, 285.3–285.62 eV, 286.9–286.97 eV, 288.57–288.68 eV and 290.29–290.48 eV, which were ascribed to graphitic carbon (C−C/H), carbon present in alcohol, ether, phenolic groups (C−O), carbonyl groups (C=O), ester or carboxyl groups (COOH) and shake-up satellite peaks owing to π-π* transitions in aromatic rings (π-π), respectively [5,55,56]. Once loaded Mn and Co species, the ratios of COOH and C=O enhanced, while the ratio of C-O decreased. The former might be associated with the loading nitrate precursors, whereas the later could be related to the desorption of C−O in high temperature calcination process under $N_2$ [5,57]. After the reactions, the ratio of total oxygen-containing functional groups raised, in which the ratio of COOH increased sharply, while the ratio of C−O declined apparently. It was reported that COOH and C=O could facilitate mercury oxidation and electron transfer on AC surface, in which they might act as chemisorption centers for $Hg^0$ [58].

The Mn 2p XPS spectra of fresh 15%Mn/BAC, fresh and used 15%CoMn/BAC samples were illustrated in Fig. 7c. The Mn 2p profile exhibited two peaks at approximately 653.5 and 642 eV, which was associated with Mn 2p 1/2 and Mn 2p 3/2 states, respectively [34]. The Mn 2p 3/2 speak could be further deconvoluted into three characteristic peaks centered at 644.4–645 eV, 642.2–642.7 eV, and 640.9–641.4 eV, which were attributed to $Mn^{4+}$, $Mn^{3+}$ and $Mn^{2+}$, respectively [25,59]. This demonstrated that $Mn^{4+}$, $Mn^{3+}$ and $Mn^{2+}$ coexisted in these samples. In this study, the ratios of $Mn^{4+}$, $Mn^{3+}$, and $Mn^{2+}$ were calculated by $Mn^{4+}/Mn^{n+}$($Mn^{n+} = Mn^{4+} + Mn^{3+} + Mn^{2+}$), $Mn^{3+}/Mn^{n+}$, and $Mn^{2+}/Mn^{n+}$, respectively. As depicted in Fig. 7c, after incorporating of $CoO_x$ into 15%Mn/BAC, all characteristic peaks corresponded to Mn species shifted to lower binding energy to some extent, and the ratios of $Mn^{4+}$, $Mn^{4+} + Mn^{3+}$, $Mn^{4+}/Mn^{3+}$ showed an upward trend, contrarily, which all demonstrated a descending tendency after the reactions. The former phenomenon indicated that the introduction of $CoO_x$ could boost the transformation of Mn species into high valence, whereas the latter appearance suggested that high valence manganese species might shift

into low valence in the reactions. Obviously, the evident decline of the ratio of $Mn^{3+}$ should be responsible for that because $Co_3O_4$ spinel structure was beneficial for the change of $Mn^{3+}$ species to $Mn^{4+}$ species [40]. It had demonstrated that high valence manganese especially $Mn^{4+}$ and its redox cycle might be conducive to high catalytic activity, thus promoting NO and $Hg^0$ removal [26,33,34,36,53,59].

The Co 2p XPS spectra of fresh and used 15%CoMn/BAC were displayed in Fig. 7d, and they exhibited two distinct peaks appeared at about 796.3 and 780.8 eV, which were assigned to Co 2p$_{1/2}$ and Co 2p$_{3/2}$ spin-orbital peaks, respectively [26,40]. Further, they could be decomposed into five type contributions including two spin-orbit doublets ($D_1$ and $D_2$) and three satellite peaks ($S_1$, $S_2$ and $S_3$). The $D_1$ contributions located at 780.8–780.6 eV and 795.9–795.7 eV could be attributed to 2p$_{3/2}$ and 2p$_{1/2}$ of octahedral $Co^{3+}$ species, while the $D_2$ contributions situated at 782.3 and 798.2 eV could be ascribed to 2p$_{3/2}$ and 2p$_{1/2}$ of tetrahedral $Co^{2+}$ species, respectively [40,60,61]. This demonstrated that both $Co^{3+}$ and $Co^{2+}$ species existed in fresh and used samples. As shown in Fig. 7d, it was clearly seen that the ratio of $Co^{3+}/Co^{2+}$ decreased from 1.27 to 0.96 after the reactions, indicating some $Co^{3+}$ had been consumed due to the transfer from $Co^{3+}$ to $Co^{2+}$. It was generally accepted that more $Co^{3+}$ species meant better redox properties of Co-based catalysts, leading to an augmentation of catalytic activity [26,62]. Furthermore, Meng et al. reported that the presence of $Co^{3+}$ species were beneficial for $NH_3$ chemisorption, thus resulting in $E_{NO}$ enhancement [63]. In this regard, we could infer that $Co^{3+}$ species played positive effects on catalytic activity.

The Hg 4f XPS spectra of used 15%CoMn/BAC were shown in Fig. 7e, which exhibited three peaks centered at 104.4, 103.4, and 101.4 eV. The medium peak was assigned to Si 2p [64,65], which was in line with XRD results. The higher binding energy peak was related to Hg 4f5/2, and the lower binding energy peak corresponded to Hg 4f7/2, which were ascribed to HgO [65–67]. Additionally, as shown in Fig. 8, the mercury conversion tests also affirmed that catalytic oxidation contributed to $Hg^0$ removal, generating HgO in the process. It was seen that no obvious peak appeared at 99.9 eV was detected, which was the characteristic peak associated with Hg 4f 7/2 for $Hg^0$ [65,67], indicating that no adsorbed $Hg^0$ were detected on the sample surface. Although adsorption including physisorption and chemisorption as well as catalytic oxidation did contribute to $Hg^0$ removal over modified ACs [2,5], even if some $Hg^0$ was adsorbed, most of which might be flushed away in the pretreatment phase of XPS measurement and residuary one might be below the detection limit [53,54]. Similar phenomenon was also observed in other works [2,65,67].

### 3.1.7. FTIR analysis

FTIR experiments were conducted to reveal the adsorbed species after different reactant molecules adsorption, exploring the $NH_3$-SCR mechanism and possible effects of $H_2O$ and $SO_2$. As presented in Fig. 9, some similar spectra emerged in all samples, which might be associated with the nature of BAC. For example, the band appeared at 3742 cm$^{-1}$ was attributed to typical hydroxyl groups [68].

After NO + $O_2$ adsorption, several new emerging bands at 1120, 1192, 1385, 1555, 1630, 2365 cm$^{-1}$ were detected. The bands at 1120 and 1192 cm$^{-1}$ might correspond to NO$^-$ [69]. The band at 1385 cm$^{-1}$ could be ascribed to nitrate species [2,19]. The obvious band at 1555 cm$^{-1}$ was attributed to NO$_3^-$ [69]. The feeble band at 1630 cm$^{-1}$ was assigned to the characteristic band of gas phase or weekly adsorbed NO$_2$ [3,69]. The band at 2365 cm$^{-1}$ might be in line with combination and overtone vibrations of nitrato species [2,19]. Several new bands at 1129, 1196, 1406, 1565 cm$^{-1}$ were observed in the spectra of $NH_3$ + $O_2$ adsorption. Thereinto, the bands at 1129, 1196 and 1406 cm$^{-1}$ represented coordinated $NH_3$ species linked to Lewis acid sites [19,26], whereas the peak at 1456 cm$^{-1}$ could be attributed to $NH_4^+$ bound to Brønsted acid sites [26]. That manifested that both Brønsted and Lewis acid sites might boost $NH_3$ adsorption and activation, promoting NO removal. Moreover, the obvious band at 1565 cm$^{-1}$
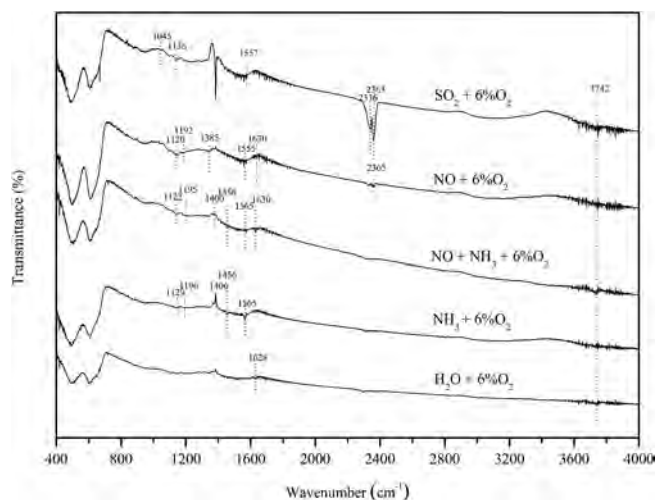
**Fig. 9.** FTIR spectra for 15%CoMn/BAC. Reaction conditions: NO + O$_2$ (500 ppm NO + 6% O$_2$), NH$_3$ + O$_2$ (500 ppm NH$_3$ + 6% O$_2$), NO + NH$_3$ + O$_2$ (500 ppm NO + 500 ppm NH$_3$ + 6% O$_2$), SO$_2$ + O$_2$ (300 ppm SO$_2$ + 6% O$_2$), H$_2$O + O$_2$ (5 vol.% H$_2$O + 6% O$_2$) and N$_2$ as balance gas.

implied the presence of amide species (–NH$_2$) [4,26]. With regard to co-adsorption of NO + NH$_3$ + O$_2$, the bands at 1122, 1195 and 1400 cm$^{-1}$ might be assigned to the overlapping of NO$^-$ and coordinated NH$_3$ species linked to Lewis acid sites [26,69]. The band at 1456 cm$^{-1}$ could be ascribed to coordinated NH$_4$$^+$ on Brønsted acid sites [40]. Similarly, the band at 1565 cm$^{-1}$ was considered as the characteristic band of –NH$_2$ [4,26]. The weak band at 1630 cm$^{-1}$ was assigned to the characteristic band of gas phase or weekly adsorbed NO$_2$ [3,69]. It was worth mentioning that the adsorption behaviors of NO and NH$_3$ over 15%CoMn/BAC in this work were consistent with the corresponding results of in situ DRIFTS tests on Mn$_x$Co$_{3-x}$O$_4$ nanocages [26].

Several characteristic bands were recorded in the SO$_2$ + O$_2$ adsorption spectra. The band arose at 1045 cm$^{-1}$ might belong to stretching vibrations from adsorbed bisulfates or sulfates, which could improve catalyst' acidity and facilitate NH$_3$ adsorption and activation, thus partly offsetting the detrimental influence of SO$_2$ [2,19]. The characteristic band appeared at 1557 cm$^{-1}$ suggested the formation of surface water that might be from the reactions between hydroxyl groups and SO$_2$ [19,68]. Moreover, the band emerged at 1136 cm$^{-1}$ was gas-phase SO$_2$, whereas two evident bands observed at 2336 and 2363 cm$^{-1}$ were in line with liquidlike physisorbed SO$_2$ [2,19]. Such adsorbed SO$_2$ might occupy limited adsorption or catalytic sites by competing with NO, NH$_3$, Hg$^0$ and O$_2$, thus restricting NO and Hg$^0$ removal, as displayed in Fig. 13. As for H$_2$O + O$_2$ adsorption spectra, the weak band detected at 1628 cm$^{-1}$ was demonstrated as the characteristic band corresponded to the $\delta_{HOH}$ of H$_2$O [2,19]. The hydrophobic property of BAC might lessen adsorbed water on the catalyst surface, thus reducing the negative influence from H$_2$O [2,28,29].

### 3.1.8. TG analysis

Fig. 10 revealed the TG-DTG curves of fresh and used 15%CoMn/BAC and 15%Mn/BAC. Both fresh 15%CoMn/BAC and 15%Mn/BAC displayed two obvious weigh losses, and the DTG curves presented two corresponding valleys. The first one existed at about 80 °C, which was attributed to the evaporation of water [70]. The second one appeared in high temperature range, which was associated with the phase transformation of metal oxides [71]. The weight losses of used 15%CoMn/BAC were mainly divided into four steps. The first step (50–100 °C) was ascribed to the desorption of water [70]. The second step (200–400 °C) was stemmed from the decomposition of (NH$_4$)$_2$SO$_4$ (230 °C) and NH$_4$HSO$_4$ (350 °C) [72], which were less than those of used 15%Mn/BAC, indicating the generation ammonia sulfates (bisulfates) was

inhibited owing to the addition of Co. Jiang et al uncovered that Mn$_{0.66}$Co$_{0.34}$-MOF-74 displayed outstanding resistance to SO$_2$ and the reason was that the incorporation of Co could weaken SO$_2$ adsorption strength on the catalyst surface [73]. The third step (500–700 °C) was related to the phase transformation of metal oxides [71]. The fourth step (around 816 °C) was assigned to the decomposition of Co$_3$O$_4$ and cobalt sulfate [74], which did not exist in used 15%Mn/BAC, suggesting Co might preferentially react with SO$_2$, thus protecting manganese active sites [70]. Moreover, the weight loss of 15%CoMn/BAC-SO$_2$ (about 16%) was much less than that of 15%Mn/BAC-SO$_2$ (about 53%). This results further demonstrated the emerging surface sulfates on used 15%CoMn/BAC was much lower than that of used 15%Mn/BAC, and the addition of Co into 15%Mn/BAC significantly enhanced its resistance to SO$_2$.

### 3.2. The performance of samples

#### 3.2.1. Effect of active ingredient

Fig. 11 demonstrated the performances of virgin BAC and modified BACs with various active ingredients for NO and Hg$^0$ simultaneous removal in the temperature range of 80–320 °C. It was of interest to note that virgin BAC exhibited the worst performance, and modified BACs with CoO$_x$ or MnO$_x$ could dramatically promote NO and Hg$^0$ removal, which indicated active ingredients had a favourable effect on the improvement of E$_{Hg}$ and especially E$_{NO}$. Compared with 15%Co/BAC and 15%Mn/BAC, 15%CoMn/BAC acquired better E$_{NO}$ and E$_{Hg}$ with a broader active temperature range, which might be ascribed to the synergistic effect between MnO$_x$ and CoO$_x$, which could promote each other and contribute to the enhancement of redox ability and the amount and dispersion of available surface active species [30]. As displayed in Fig. 11b, E$_{NO}$ and E$_{Hg}$ of XCoMn/BACs manifested various trend with the augment of reaction temperature. Thereinto, except for 7.5%CoMn/BAC, E$_{NO}$ and E$_{Hg}$ of which increased until 280 °C and then descended at 320 °C. E$_{NO}$ of others shared an apparent enhancement in the temperature range of 80 °C–240 °C and therewith yielded an obvious decline. However, E$_{Hg}$ exhibited a slight ascension with the increase of reaction temperature from 80 °C to 240 °C, and afterwards showed an evident decrease with further increasing reaction temperature. Meanwhile, 15%CoMn/BAC exhibited better E$_{Hg}$ than other samples, while 15%CoMn/BAC and 22.5%CoMn/BAC acquired optimal E$_{NO}$, and 15%CoMn/BAC yielded the best E$_{Hg}$ of 98.5% and the highest E$_{NO}$ of 86.5% at 240 °C. Based on BET results, it seemed pretty clear that both E$_{NO}$ and E$_{Hg}$ of XCoMn/BACs were not invariably in line with BET surface areas and total pore volumes, revealing that physisorption had a definite but not decisive effect on NO and Hg$^0$ removal. Owing to comprehensive consideration, 15%CoMn/BAC was chosen for subsequent study in this work.

It was well recognized that reaction temperature played a critical role in catalytic reactions and there was a corresponding active temperature range for a given catalyst and reaction, before which catalytic activity would boost with the increase of reaction temperature due to the improvement of catering activation energy [2,65]. Moreover, reaction temperature enhancement might also promote chemisorption owing to forming more chemical bonds [2,75]. That might be responsible for the increases of E$_{NO}$ and E$_{Hg}$ with the increase of reaction temperature. The evident decreases of E$_{NO}$ and E$_{Hg}$ at high temperature might be possibly explained by several reasons. One reason for those decreases could be explained by that the adsorption of reactant molecules like Hg$^0$ might be inhibited by high temperature [2,76]. In addition, the other one might be attributed to the structure damage of BAC resulted from metal oxides catalytic oxidizing carbon matrix [2,5,77].

#### 3.2.2. Effect of O$_2$ concentration

The effect of O$_2$ concentration on NO and Hg$^0$ simultaneous removal over 15%CoMn/BAC were illustrated in Fig. 12. The sample only
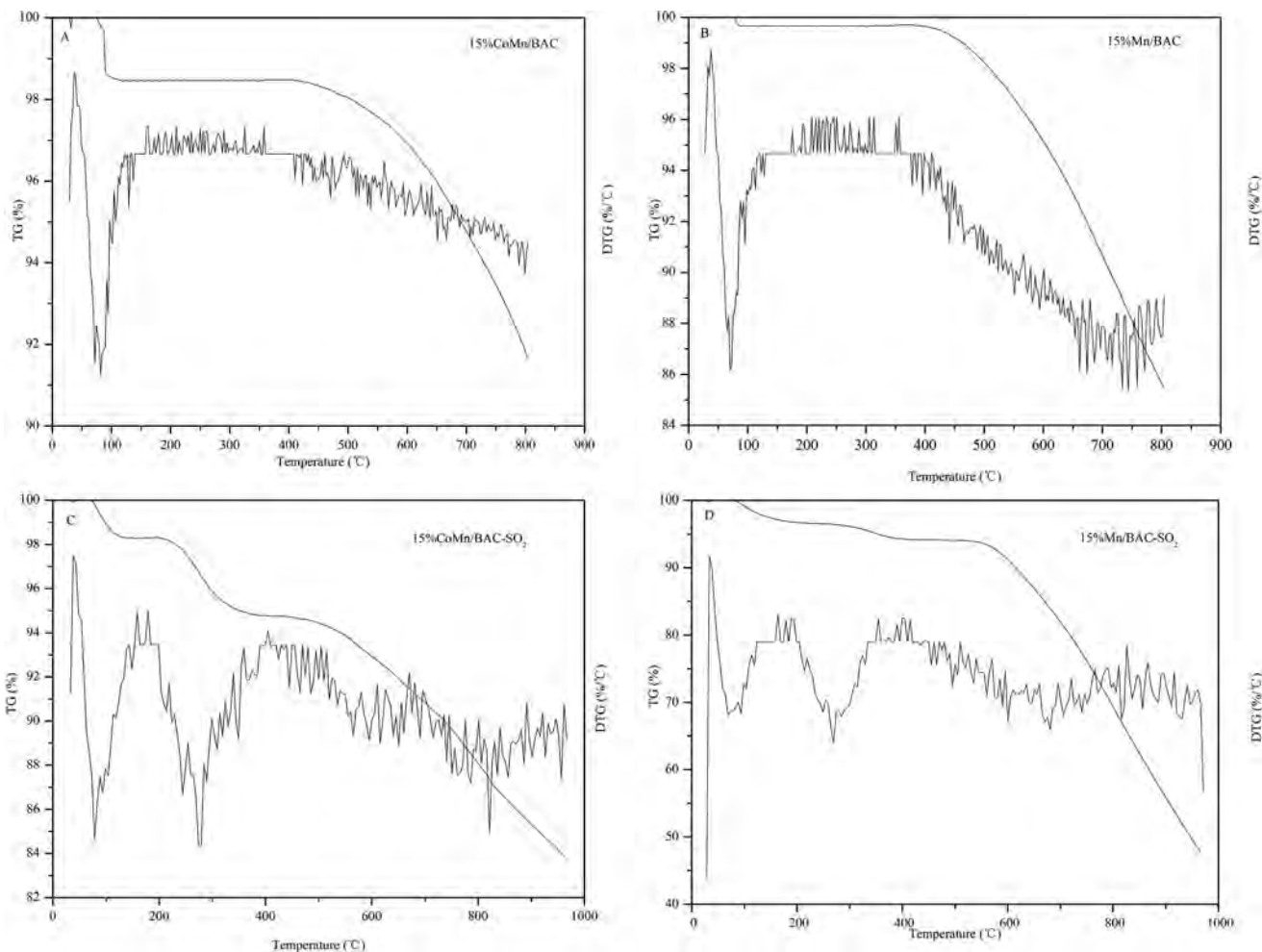
**Fig. 10.** TG-DTG profiles of the catalysts: fresh 15%CoMn/BAC (A), fresh 15%Mn/BAC (B), used 15%CoMn/BAC-SO$_2$ (C), used 15%Mn/BAC-SO$_2$ (D).
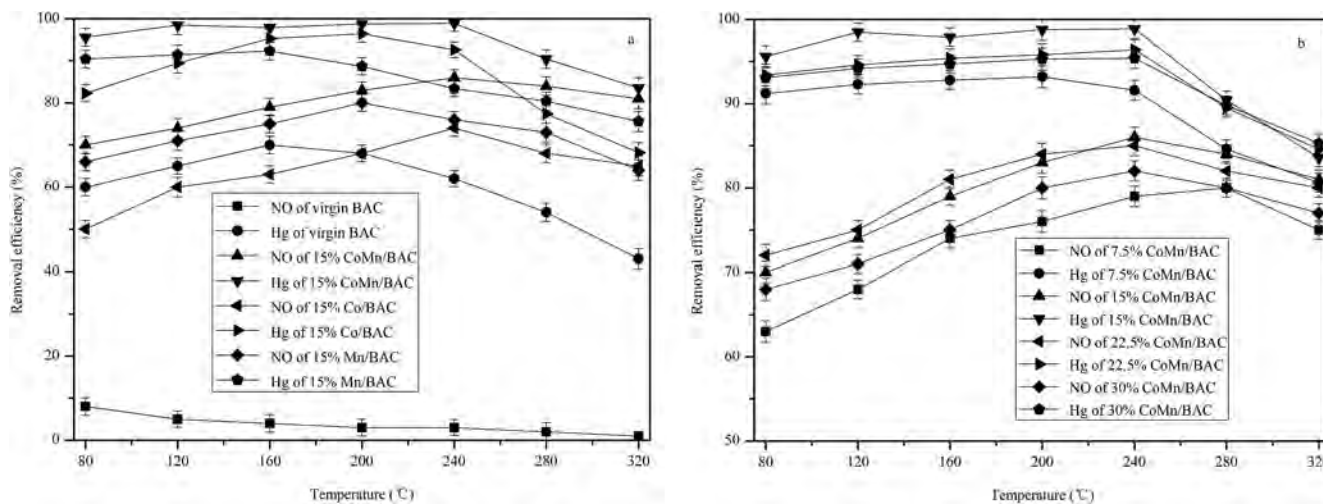


**Fig. 11.** Effect of active ingredients on simultaneous NO and Hg$^0$ removal over virgin BAC and modified BACs. (a) The performance of simultaneous NO and Hg$^0$ removal over virgin BAC, 15%Mn/BAC, 15%Co/BAC and 15%CoMn/BAC; (b) The performance of simultaneous NO and Hg$^0$ removal over 7.5%–30%CoMn/BACs. Reaction conditions: T = 80–320 °C, 6% O$_2$, 100 µg/m$^3$ Hg$^0$, 500 ppm NO, 500 ppm NH$_3$, N$_2$ as balance.

possessed $E_{NO}$ of 12% and $E_{Hg}$ of 51% in the absence of O$_2$, and the poor performance might mainly come from adsorption and weak reactions due to the preexisting O$_\alpha$ and O$_\beta$, as discussed in the O 1s XPS analysis. When 3%O$_2$ was added into the flue gas, $E_{NO}$ and $E_{Hg}$ achieved a significant improvement from 12% and 51% to 81% and 92%,

respectively. Furthermore, $E_{NO}$ and $E_{Hg}$ obtained a slight further enhance after the addition of 6% O$_2$, and the further increases of $E_{NO}$ and $E_{Hg}$ became negligible when O$_2$ concentration augmented from 6% to 9% or even to 12%. This phenomenon indicated gaseous O$_2$ could observably facilitate NO and Hg$^0$ removal when flue gas was short of
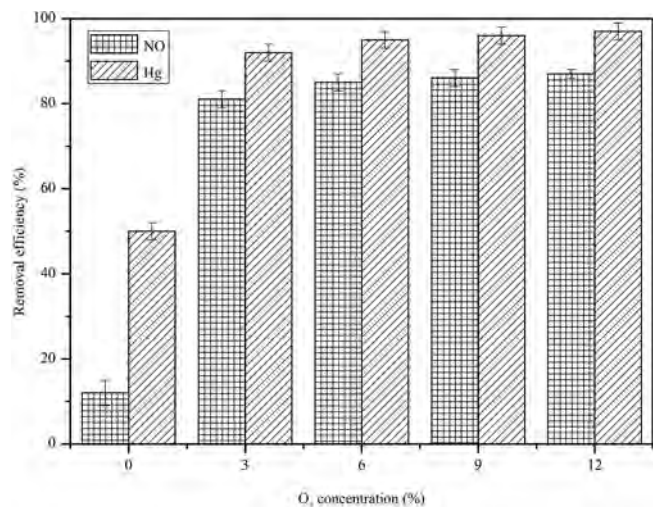
**Fig. 12.** The effect of $O_2$ concentration on simultaneous NO and $Hg^0$ removal over 15%CoMn/BAC. Reaction conditions: T = 240 °C, 0–12% $O_2$, 100 μg/m³ $Hg^0$, 500 ppm NO, 500 ppm $NH_3$, $N_2$ as balance.

enough oxygen, which could be explained by that gaseous $O_2$ could replenish consumed $O_\beta$ and $O_\alpha$ in NO and $Hg^0$ removal reactions, thus keeping such reactions continuously proceeding, in which oxygen vacancies and lattice defects on sample surface were conducive to $O_2$ activation and adsorption [62], and they were beneficial for the oxidation of NO–$NO_2$, promoting NO reduction and $Hg^0$ oxidation [30,53]. Fortunately, it was inferred that $O_2$ concentration in practical coal-fired flue gas was often sufficient for continuous reactions.

### 3.2.3. Effect of $SO_2$ and $H_2O$

The single and congregate effects of $SO_2$ and $H_2O$ on the simultaneous removal of NO and $Hg^0$ over 15%CoMn/BAC were displayed in Fig. 13. It was observed that both $SO_2$ and $H_2O$ had negative effects on $Hg^0$ and NO removal, and the detrimental influences increased with the enhancement of $SO_2$ and $H_2O$ concentrations. For instance, when 300 ppm $SO_2$ was added into the flue gas, $E_{Hg}$ decreased from 97.4% to 95.2%, while $E_{NO}$ declined to 82.3% from 86.3%. It was worth mentioning that in preliminary experiments 300 ppm $SO_2$ could cause $E_{Hg}$ and $E_{NO}$ of 15%Mn/BAC to drop by about 23% and 18%, respectively.
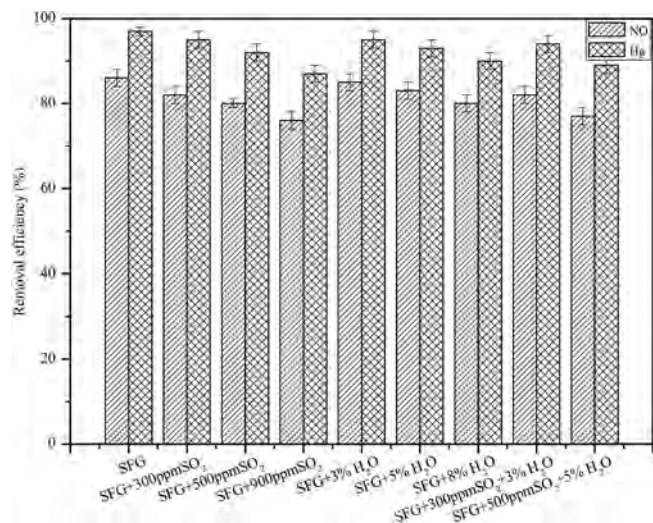


**Fig. 13.** The separate or synchronous effects of $SO_2$ and $H_2O$ on simultaneous NO and $Hg^0$ removal over 15%CoMn/BAC. Reaction conditions: T = 240 °C, 6% $O_2$, 100 μg/m³ $Hg^0$, 500 ppm NO, 500 ppm $NH_3$, 300–900 ppm $SO_2$ (when used), 3–8 vol.% $H_2O$ (when used), $N_2$ as balance.

That demonstrated that $CoO_x$ modified 15%Mn/BAC could significantly enhance its $SO_2$ resistance, which might be attributed to two reasons. One reason was the introduction of Co inhibiting the generating ammonia sulfates (bisulfates) by weakening $SO_2$ adsorption strength on the catalyst surface [73]. The other one might be related to that the introduction of Co could preferentially react with $SO_2$, thus protecting manganese active sites [70]. Combined with literature and FTIR analysis, two reasons could be responsible for the inhibitory effect of $SO_2$. For one thing, $SO_2$ might be in competition with $Hg^0$, NO and $NH_3$ for catalytic or adsorption sites [2,78]. For another, the possible generation of ammonium sulfates or bisulfates would destroy the porous structure and cover activated sites, besides, the formation of metal sulfates might lead metal catalytic sites to inactive phases [2,68], thus causing the decreases of $E_{NO}$ and $E_{Hg}$.

Likewise, $E_{NO}$ and $E_{Hg}$ were slightly inhibited by $H_2O$(g), and 8% $H_2O$ could induce $E_{NO}$ to fall by 5.1% from 86.3% to 81.2%, and $E_{Hg}$ to drop by 6.9% from 97.4 to 90.5%, suggesting that 15%CoMn/BAC yielded excellent $H_2O$ resistance, which might be related to the hydrophobic property of BAC and the strong interaction between $MnO_x$ and $CoO_x$ species [27–29]. Similarly, the inhibitive effect might probably result from the competitive adsorption among $H_2O$, NO, $NH_3$ and $Hg^0$ for adsorption or catalytic sites [76,79]. What's more, the synchronous additions of $SO_2$ and $H_2O$ contributed to more obvious drops of $E_{NO}$ and $E_{Hg}$ than that of single effects of $SO_2$ and $H_2O$. It was noteworthy that 15%CoMn/BAC still displayed 82%NO removal efficiency and 94% $Hg^0$ removal efficiency under SFG + 500 ppm $SO_2$ + 5% $H_2O$, and the excellent anti-$SO_2$/$H_2O$ performance preceded many reported catalysts [15,19,20,23]. For instance, 400 ppm $SO_2$ or 8% $H_2O$ could cause both $E_{NO}$ and $E_{Hg}$ over $V_2O_5$-$CeO_2$/$TiO_2$ to decline by 20% [15]. As mentioned earlier, the giant drops of $E_{NO}$ and $E_{Hg}$ could be explained by the synergistic competition for adsorption or catalytic sites among $SO_2$, $H_2O$, NO, $NH_3$ and $Hg^0$, and the possible generation of ammonium sulfates (bisulfates) or metal sulfates also gave rise to that [2,5,43].

### 3.3. The interaction between NO removal and $Hg^0$ removal

#### 3.3.1. Effect of $Hg^0$ on NO removal

It was of extraordinary significance to study whether the presence of $Hg^0$ removal affected NO removal. Therefore, interrelated tests were conducted and the results were displayed in Fig. 14. $E_{NO}$ did not manifest any distinct change when $Hg^0$ removal was suddenly interrupted by stopping the supply of $Hg^0$, and $E_{NO}$ seemed hardly changed
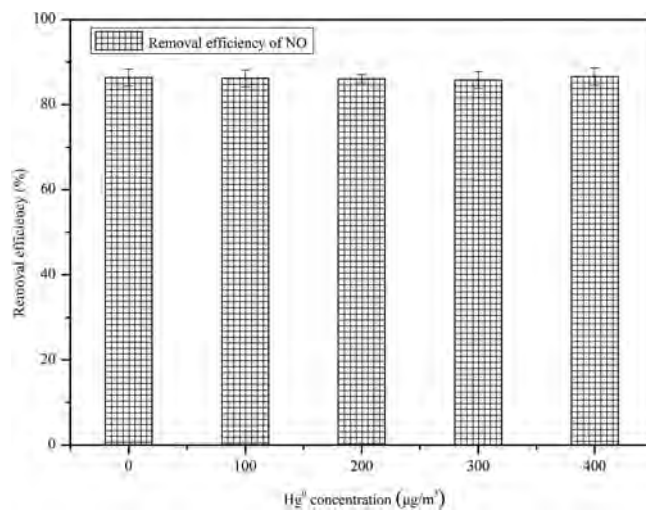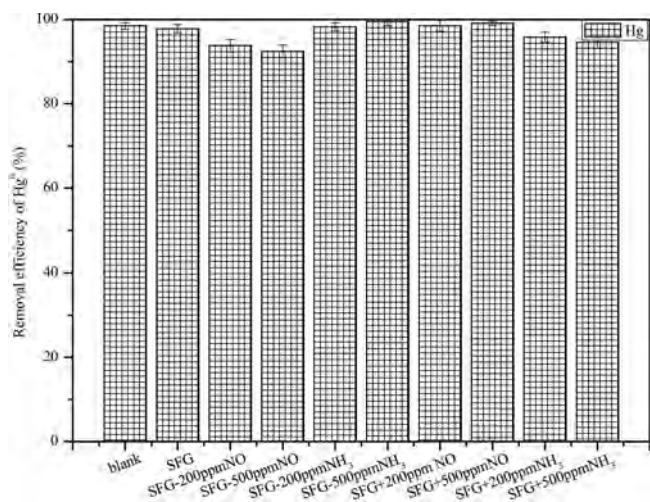


**Fig. 14.** Effect of $Hg^0$ concentration on NO removal over 15%CoMn/BAC. Reaction conditions: T = 240 °C, 6% $O_2$, 0–400 μg/m³ $Hg^0$, 500 ppm NO, 500 ppm $NH_3$, $N_2$ as balance.
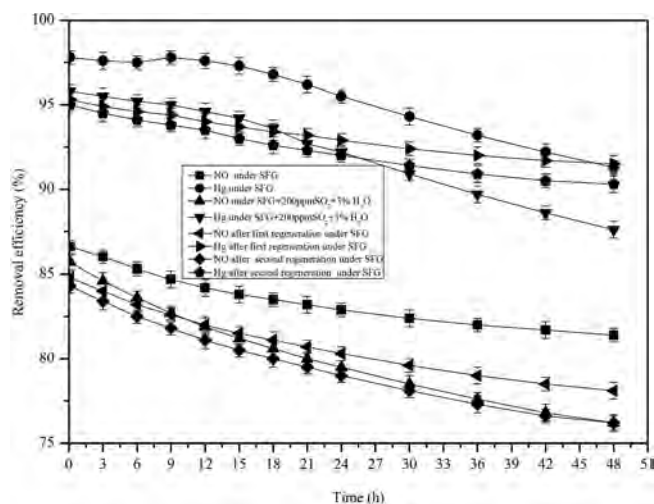
**Fig. 15.** Effect of SCR atmosphere ($NH_3$ and NO) on $Hg^0$ removal over 15%CoMn/BAC. Reaction conditions: T = 240 °C, 6% $O_2$, 100 µg/m³ $Hg^0$, 0–1000 ppm NO, 0–1000 ppm $NH_3$, $N_2$ as balance.



**Fig. 16.** The stability and recyclability of 15%CoMn/BAC for simultaneous NO and $Hg^0$ removal. Reaction conditions: T = 240 °C, 6% $O_2$, 100 µg/m³ $Hg^0$, 500 ppm NO, 500 ppm $NH_3$, 200 ppm $SO_2$ (when used), 3 vol.% $H_2O$ (when used), $N_2$ as balance.

even if 100 µg/m³ $Hg^0$ was rejoined. Nevertheless, $E_{NO}$ exhibited a trifling decrease with further enhancement of $Hg^0$ concentration, revealing that high concentration of $Hg^0$ could give rise to a slight prohibitive influence on NO removal. The inhibitory effect might be attributed to two possible reasons. On the one hand, $Hg^0$ could compete with NO or $NH_3$ for adsorption or catalytic sites. On the other hand, the formation of HgO as confirmed by XPS analysis and mercury conversion tests, might accumulate on sample surface and cover active sites [2,5,19,51]. And they both increased with the enhancement of $Hg^0$ concentration, thus resulting in a slight decline of $E_{NO}$. It was remarkable that $Hg^0$ concentration in actual coal-fired flue gas was much lower than the tests, and we could infer that the practical NO removal might be scarcely affected by $Hg^0$ removal.

### 3.3.2. Effect of SCR atmosphere on $Hg^0$ removal

As presented in Fig. 15, the effects of SCR atmosphere including NO and $NH_3$ on $Hg^0$ removal were inspected. For comparison, the blank test was performed to acquire the original $E_{Hg}$ without the interference of NO removal by removing NO and $NH_3$ from the SFG. It was clearly seen that original $E_{Hg}$ exhibited higher than that under SFG conditions, indicating that NO removal could have negative effect on $Hg^0$ removal, which was in good line with previous works [2,5,19]. It was speculated that NO removal might preponderate over $Hg^0$ removal under high concentrations of NO and $NH_3$ [19,80].

Fig. 15 further uncovered the individual effect of $NH_3$ and NO on $Hg^0$ removal. When 200 ppm or 500 ppm NO was subtracted from the SFG, $E_{Hg}$ exhibited an obvious drop. Similarly, $E_{Hg}$ also showed an apparent descending trend when additional 200 ppm or 500 ppm $NH_3$ was added into SFG. In other words, $NH_3$ alone and excess $NH_3$ ($NH_3$/ NO > 1) both played evidently inhibitory effect on $Hg^0$ removal, which might be ascribed to that $NH_3$ could be rapidly adsorbed to generate adsorbed $NH_3$ species, in which surface active sites were occupied and active oxygen was consumed, inhibiting $Hg^0$ oxidation and thus leading to a decrease of $E_{Hg}$ [69,81]. On the contrary, the stimulative effect of NO alone on $Hg^0$ removal was detected and the promotional appearance was also observed when $NH_3$ and superfluous NO ($NH_3$/NO < 1) coexisted in the conditions. That might be probably explained by that NO could be weakly absorbed on the sample surface, and some of adsorbed NO species might be oxidized to $NO_2$ by surface active oxygen, which was beneficial for $Hg^0$ oxidation [33,53].
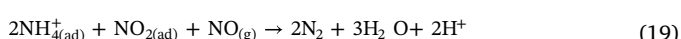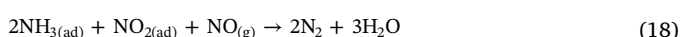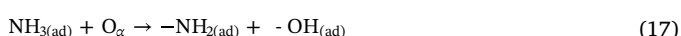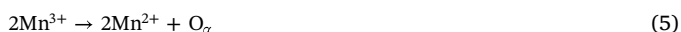
### 3.4. Stability and recyclability tests

The stability and recyclability of a given catalyst were essential factors to evaluate its industrial application potential. As shown in Fig. 16, both $E_{NO}$ and $E_{Hg}$ of 15%CoMn/BAC under SFG exhibited a slower decline than that under SFG with 200 ppm $SO_2$ and 3% $H_2O$, which was ascribed to the combined negative effects from $SO_2$ and $H_2O$ as discussed above. Notably, 15%CoMn/BAC ultimately yielded $E_{NO}$ of 80% and $E_{Hg}$ of 92.2% under SFG with 200 ppm $SO_2$ and 3% $H_2O$ after 24 h, indicating its industrial application potential.

Interestingly, the descending trends of $E_{NO}$ and $E_{Hg}$ with time were different, in which $E_{NO}$ demonstrated a continuous decrease with time, whereas $E_{Hg}$ even exhibited a mild increase at first and then decreased with time. That interesting appearance might be associated with different removal mechanisms of NO and $Hg^0$, since both catalytic oxidation and adsorption with limited adsorption capacity were conjectured to devote $Hg^0$ removal while adsorption was hardly responsible for NO removal [2,5]. Moreover, $E_{NO}$ and $E_{Hg}$ became worse with the increase of regeneration frequencies, in which the regeneration was acquired at 600 °C for 2 h under $N_2$ based on our previous works and preliminary experiments [2,5]. That might be related to two possible reasons, on one hand, the regeneration was incomplete or some adsorption and catalytic sites becoming inactive due to unreasonable regeneration temperature or other factors. On the other hand, the prolonged catalytic oxidizing BAC into CO or $CO_2$ from metal oxides would damage the pore structure and surface areas, thus causing certain drops of $E_{NO}$ and $E_{Hg}$ [2,5,77]. Thereinto, the later one might be the bottleneck of carbon-based catalysts used at higher temperature, which imposed restrictions on such catalysts' application to some extent.

## 4. Mechanism study

With regard to $NH_3$-SCR of NO over metal oxides modified AC(BAC) catalysts, it was acknowledged that metal oxides were the catalytic centers that served as the electron transfer station of reactants including $NH_3$, NO and $O_2$ [2,5,77,82,83]. In addition, it was well-known accepted that $Mn^{4+}$ was the most active species and the valence change from $Mn^{4+}$ to $Mn^{3+}$ and therewith to $Mn^{2+}$ in Mn-based catalysts was the possible mechanism for both $Hg^0$ oxidation and NO reduction [3,7,21,22]. According to characterization and experimental results and literature, possible reaction pathways were inferred as follows: $NH_3$ was

instantly coordinated to Lewis or Brønsted acid sites, forming intermediate species such as $NH_4^+$ and $-NH_2$. Meanwhile, some NO was weakly adsorbed on the sample surface and then was oxidized to $NO_2$, and gaseous NO and adsorbed $NO_2$ react with adsorbed $NH_3$ intermediate species to generate uninjurious $N_2$ and $H_2O$ [2,19,26]. These reactions were summarized as Eqs. (4)–(20), in which Mn-Co complex oxides acted as catalytic centers.

$$2Mn^{4+} \rightarrow 2Mn^{3+} + O_\alpha \tag{4}$$

$$2Mn^{3+} \rightarrow 2Mn^{2+} + O_\alpha \tag{5}$$

$$2Mn^{3+} + 1/2O_2 \rightarrow 2Mn^{4+} \tag{6}$$

$$2Mn^{2+} + 1/2O_2 \rightarrow 2Mn^{3+} \tag{7}$$

$$2Co^{3+} \rightarrow 2Co^{2+} + O_\alpha \tag{8}$$

$$2Co^{2+} + 1/2O_2 \rightarrow 2Co^{3+} \tag{9}$$

$$O_{2(g)} \rightarrow 2O_\beta \tag{10}$$

$$NO_{(g)} \rightarrow NO_{(ad)} \tag{11}$$

$$2NO_{(g)} + O_{2(g)} \rightarrow 2NO_{2(g)} \tag{12}$$

$$NO_{2(g)} \rightarrow NO_{2(ad)} \tag{13}$$

$$NO_{(ad)} + O_\alpha/O_\beta \rightarrow NO_{2(ad)} \tag{14}$$

$$NH_{3(g)} \rightarrow NH_{3(ad)} \tag{15}$$

$$NH_{3(g)} + H_{surface}^+ \rightarrow NH_{4(ad)}^+ \tag{16}$$

$$NH_{3(ad)} + O_\alpha \rightarrow -NH_{2(ad)} + {\text{-}}OH_{(ad)} \tag{17}$$

$$2NH_{3(ad)} + NO_{2(ad)} + NO_{(g)} \rightarrow 2N_2 + 3H_2O \tag{18}$$

$$2NH_{4(ad)}^+ + NO_{2(ad)} + NO_{(g)} \rightarrow 2N_2 + 3H_2O + 2H^+ \tag{19}$$

$$-NH_{2(ad)} + NO_{(g)} \rightarrow N_2 + H_2O \tag{20}$$

As for $Hg^0$ removal over metal oxides modified BAC, our previous works and mercury conversion tests demonstrated that catalytic oxidation and adsorption including physisorption and chemisorption contributed to that, whose contributions varied with reaction temperature and time. As shown in Fig. 8, the contribution from catalytic oxidation dominated gradually due to limited adsorption capacity [2,5]. The results of O 1s XPS verified that $O_\beta$ participated in NO and $Hg^0$ simultaneous removal, furthermore, both $O_\alpha$ and $O_\beta$ were deemed to take part in $Hg^0$ oxidation reactions (as shown in Eqs. (22) and (23)) [2,5,76]. Therefore, we also speculated that both $O_\alpha$ and $O_\beta$ took place that and were consumed in the process, which followed Mars-Masson mechanism [25,53,84]. It was surmised that $Hg^0(g)$ was first adsorbed and whereafter $Hg_{(ad)}^0$ was oxidized into HgO by $O_\alpha$ and $O_\beta$, moreover, adsorbed $NO_2$ might also oxidize $Hg_{(ad)}^0$ into HgO [53]. Subsequently, as shown in Eqs. (6), (7) and (9), gaseous $O_2$ reoxidized reduced metal oxides and replenished consumed $O_\alpha$ and $O_\beta$ [85]. Hence, such possible pathways could be proposed as follows:

$$Hg_{(g)}^0 \rightarrow Hg_{(ad)}^0 \tag{21}$$

$$Hg_{(ad)}^0 + O_\alpha \rightarrow HgO \tag{22}$$

$$Hg_{(ad)}^0 + O_\beta \rightarrow HgO \tag{23}$$

$$Hg_{(ad)}^0 + NO_{2(ad)} \rightarrow HgO + NO \tag{24}$$
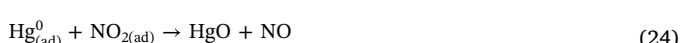
## 5. Conclusions

A series of CoMn/BACs catalysts prepared by the ultrasound-assisted impregnation method were employed for the simultaneous removal of NO and $Hg^0$. 15%CoMn/BAC exhibited outstanding performance for NO and $Hg^0$ removal in a wide temperature range from 160 to 280 °C, and it yielded prominent NO removal efficiency (86.5%) and superior $Hg^0$ removal efficiency (98.5%) at 240 °C. The interaction between NO removal and $Hg^0$ removal lessened their corresponding separate efficiencies, the adverse effect of $NH_3$ on $Hg^0$ removal could not be offset by the promotional influences of NO and $O_2$. $SO_2$ and $H_2O$ both had negative effects on NO and $Hg^0$ removal. Compared with 15% Mn/BAC, the addition of $CoO_x$ with suitable amount into 15%CoMn/BAC could contribute to the synergistic effect between $MnO_x$ and $CoO_x$, resulting in the increase of BET surface area and surface active oxygen species as well as $Mn^{4+}$ concentration, the enhancement of redox ability and the strength or amount of surface acid sites, restraining the crystallization of $MnO_x$, which might be responsible for the improvement of catalytic performance and $SO_2$ resistance. In addition, the hydrophobic property of BAC strengthened the catalyst' tolerance to $H_2O$. The results of stability and recyclability tests indicated that 15%CoMn/BAC possessed a promising application potential for NO and $Hg^0$ simultaneous removal at low temperature.

## References

[1] K. Liu, S. Wang, Q. Wu, L. Wang, Q. Ma, L. Zhang, G. Li, H. Tian, L. Duan, J. Hao, A highly resolved mercury emission inventory of Chinese coal-fired power plants, Environ. Sci. Technol. 52 (2018) 2400–2408, https://doi.org/10.1021/acs.est.7b06209.

[2] L. Gao, C. Li, J. Zhang, X. Du, S. Li, J. Zeng, Y. Yi, G. Zeng, Simultaneous removal of NO and $Hg^0$ from simulated flue gas over $CoO_x$-$CeO_2$ loaded biomass activated carbon derived from maize straw at low temperatures, Chem. Eng. J. 342 (2018) 339–349, https://doi.org/10.1016/j.cej.2018.02.100.

[3] Z. Yang, H. Li, X. Liu, P. Li, J. Yang, P.-H. Lee, K. Shih, Promotional effect of CuO loading on the catalytic activity and $SO_2$ resistance of $MnO_x$/$TiO_2$ catalyst for simultaneous NO reduction and $Hg^0$ oxidation, Fuel 227 (2018) 79–88, https://doi.org/10.1016/j.fuel.2018.04.074.

[4] Y. Li, X. Han, Y. Hou, Y. Guo, Y. Liu, Y. Cui, Z. Huang, Role of CTAB in the improved $H_2O$ resistance for selective catalytic reduction of NO with $NH_3$ over iron titanium catalyst, Chem. Eng. J. 347 (2018) 313–321, https://doi.org/10.1016/j.cej.2018.04.107.

[5] L. Gao, C. Li, P. Lu, J. Zhang, X. Du, S. Li, L. Tang, J. Chen, G. Zeng, Simultaneous removal of $Hg^0$ and NO from simulated flue gas over columnar activated coke granules loaded with $La_2O_3$-$CeO_2$ at low temperature, Fuel 215 (2018) 30–39, https://doi.org/10.1016/j.fuel.2017.11.008.

[6] H. Xu, Z. Qu, C. Zong, F. Quan, J. Mei, N. Yan, Catalytic oxidation and adsorption of $Hg^0$ over low-temperature $NH_3$-SCR $LaMnO_3$ perovskite oxide from flue gas, Appl. Catal., B 186 (2016) 30–40, https://doi.org/10.1016/j.apcatb.2015.12.042.

[7] C. Liu, F. Li, J. Wu, X. Hou, W. Huang, Y. Zhang, X. Yang, A comparative study of $MO_x$ (M = Mn, Co and Cu) modifcations over $CePO_4$ catalysts for selective catalytic reduction of NO with $NH_3$, J. Hazard. Mater. 363 (2019) 439–446, https://doi.org/10.1016/j.jhazmat.2018.09.054.

[8] L. Xu, S. Niu, C. Lu, Q. Zhang, J. Li, Influence of calcination temperature on $Fe_{0.8}Mg_{0.2}O_z$ catalyst for selective catalytic reduction of $NO_x$ with $NH_3$, Fuel 219 (2018) 248–258, https://doi.org/10.1016/j.fuel.2018.01.083.

[9] Z. Fan, J.-W. Shi, C. Gao, G. Gao, B. Wang, Y. Wang, C. He, C. Niu, Gd-modified $MnO_x$ for the selective catalytic reduction of NO by $NH_3$: the promoting effect of Gd on the catalytic performance and sulfur resistance, Chem. Eng. J. 348 (2018) 820–830, https://doi.org/10.1016/j.cej.2018.05.038.

[10] B. Zhao, R. Ran, X. Guo, L. Cao, T. Xu, Z. Chen, X. Wu, Z. Si, D. Weng, Nb-modified Mn/Ce/Ti catalyst for the selective catalytic reduction of NO with $NH_3$ at low temperature, Appl. Catal., A 545 (2017) 64–71, https://doi.org/10.1016/j.apcata.2017.07.024.

[11] B. Shen, B. Zhu, X. Zhang, G. Chi, D. Patel, M. Si, C. Wu, Simultaneous removal of NO and $Hg^0$ using Fe and Co co-doped Mn-Ce/$TiO_2$ catalysts, Fuel 224 (2018) 241–249, https://doi.org/10.1016/j.fuel.2018.03.080.

[12] X. Zhang, Y. Cui, J. Wang, B. Tan, C. Li, H. Zhang, G. He, Simultaneous removal of $Hg^0$ and NO from flue gas by $Co_{0.3}$-$Ce_{0.35}$-$Zr_{0.35}O_2$ impregnated with $MnO_x$, Chem. Eng. J 326 (2017) 1210–1222, https://doi.org/10.1016/j.cej.2017.06.014.

[13] S. Zhang, Y. Zhao, J. Yang, J. Zhang, C. Zheng, Fe-modified $MnO_x$/$TiO_2$ as the SCR catalyst for simultaneous removal of NO and mercury from coal combustion flue gas, Chem. Eng. J. 348 (2018) 618–629, https://doi.org/10.1016/j.cej.2018.05.037.

[14] Y. Gao, Z. Zhang, J. Wu, L. Duan, A. Umar, L. Sun, Z. Guo, Q. Wang, A critical review on the heterogeneous catalytic oxidation of elemental mercury in flue gases, Environ. Sci. Technol. 47 (2013) 10813–10823, https://doi.org/10.1021/es402495h.

[15] X. Zhang, C. Li, L. Zhao, J. Zhang, G. Zeng, Y. Xie, M. Yu, Simultaneous removal of elemental mercury and NO from flue gas by V₂O₅–CeO₂/TiO₂ catalysts, Appl. Surf. Sci. 347 (2015) 392–400, https://doi.org/10.1016/j.apsusc.2015.04.039.

[16] B. Yang, Z. Li, Q. Huang, M. Chen, L. Xu, Y. Shen, S. Zhu, Synergetic removal of elemental mercury and NO over TiCe₀.₂₅Sn₀.₂₅Oₓ catalysts from flue gas: performance and mechanism study, Chem. Eng. J. 360 (2019) 990–1002, https://doi.org/10.1016/j.cej.2018.09.193.

[17] X. Zhang, B. Shen, F. Shen, X. Zhang, M. Si, P. Yuan, The behavior of the manganese-cerium loaded metal-organic framework in elemental mercury and NO removal from flue gas, Chem. Eng. J. 326 (2017) 551–560, https://doi.org/10.1016/j.cej.2017.05.128.

[18] H. Li, S. Wang, X. Wang, J. Hu, Activity of CuCl₂-modified cobalt catalyst supported on Ti-Ce composite for simultaneous catalytic oxidation of Hg⁰ and NO in a simulated pre-sco process, Chem. Eng. J. 316 (2017) 1103–1113, https://doi.org/10.1016/j.cej.2017.02.052.

[19] J. Zhang, C. Li, L. Zhao, T. Wang, S. Li, G. Zeng, A sol-gel Ti-Al-Ce-nanoparticle catalyst for simultaneous removal of NO and Hg⁰ from simulated flue gas, Chem. Eng. J. 313 (2017) 1535–1547, https://doi.org/10.1016/j.cej.2016.11.039.

[20] L.-Y. Lin, C.-Y. Lee, Y.-R. Zhang, H. Bai, Aerosol-assisted deposition of Mn-Fe oxide catalyst on TiO₂ for superior selective catalytic reduction of NO with NH₃ at low temperatures, Catal. Commun. 111 (2018) 36–41, https://doi.org/10.1016/j.catcom.2018.02.019.

[21] W. Xu, G. Zhang, H. Chen, G. Zhang, Y. Han, Y. Chang, P. Gong, Mn/beta and Mn/ZSM-5 for the low-temperature selective catalytic reduction of NO with ammonia: effect of manganese precursors, Chin. J. Catal. 39 (2018) 118–127, https://doi.org/10.1016/S1872-2067(17)62983-8.

[22] C. He, B. Shen, J. Chen, J. Cai, Adsorption and oxidation of elemental mercury over Ce-MnOₓ/Ti-PILCs, Environ. Sci. Technol. 48 (2014) 7891–7898, https://doi.org/10.1021/es5007719.

[23] S. Zhang, Y. Zhao, J. Yang, Y. Zhang, P. Sun, X. Yu, J. Zhang, C. Zheng, Simultaneous NO and mercury removal over MnOₓ/TiO₂ catalyst in different atmospheres, Fuel Process. Technol. 166 (2017) 282–290, https://doi.org/10.1016/j.fuproc.2017.06.011.

[24] S. Zhang, Y. Zhao, Z. Wang, J. Zhang, L. Wang, C. Zheng, Integrated removal of NO and mercury from coal combustion flue gas using manganese oxides supported on TiO₂, J. Environ. Sci. 53 (2017) 141–150, https://doi.org/10.1016/j.jes.2015.10.038.

[25] J. Yang, Y. Zhao, J. Zhang, C. Zheng, Regenerable cobalt oxide loaded magnetosphere catalyst from fly ash for mercury removal in coal combustion flue gas, Environ. Sci. Technol. 48 (2014) 14837–14843, https://doi.org/10.1021/es504419v.

[26] L. Zhang, L. Shi, L. Huang, J. Zhang, R. Gao, D. Zhang, Rational design of high-performance deNOx catalysts based on MnₓCo₃₋ₓO₄ nanocages derived from metal−organic frameworks, ACS Catal. 4 (2014) 1753–1763, https://doi.org/10.1021/cs401185c.

[27] L.F. Liotta, H. Wu, G. Pantaleo, A.M. Venezia, Co₃O₄ nanocrystals and Co₃O₄–MOₓ binary oxides for CO, CH₄ and VOC oxidation at low temperatures: a review, Catal. Sci. Technol. 3 (2013) 3085–3102, https://doi.org/10.1039/c3cy00193h.

[28] Z. Abdelouahab-Reddam, R. El Mail, F. Coloma, A. Sepúlveda-Escribano, Platinum supported on highly-dispersed ceria on activated carbon for the total oxidation of VOCs, Appl. Catal., A 494 (2015) 87–94, https://doi.org/10.1016/j.apcata.2015.01.026.

[29] H.-J. Joung, J.-H. Kim, J.-S. Oh, D.-W. You, H.-O. Park, K.-W. Jung, Catalytic oxidation of VOCs over CNT-supported platinum nanoparticles, Appl. Surf. Sci. 290 (2014) 267–273, https://doi.org/10.1016/j.apsusc.2013.11.066.

[30] H. Chen, Y. Xia, H. Huang, Y. Gan, X. Tao, C. Liang, J. Luo, R. Fang, J. Zhang, W. Zhang, X. Liu, Highly dispersed surface active species of Mn/Ce/TiW catalysts for high performance at low temperature NH₃-SCR, Chem. Eng. J. 330 (2017) 1195–1202, https://doi.org/10.1016/j.cej.2017.08.069.

[31] Y. Liu, N. Sun, S. Chen, R. Yan, P. Li, Y. Qu, Y. Qu, L. Jing, Synthesis of nano SnO₂-coupled mesoporous molecular sieve titanium phosphate as a recyclable photocatalyst for efficient decomposition of 2,4-dichlorophenol, Nano Res. 11 (2018) 1612–1624, https://doi.org/10.1007/s12274-017-1776-z.

[32] B. Guan, H. Lin, L. Zhu, B. Tian, Z. Huang, Effect of ignition temperature for combustion synthesis on the selective catalytic reduction of NOₓ with NH₃ over Ti₀.₉Ce₀.₀₅V₀.₀₅O₂₋δ nanocomposites catalysts prepared by solution combustion route, J Chem. Eng. 181–182 (2012) 307–322, https://doi.org/10.1016/j.cej.2011.11.083.

[33] J. Li, N. Yan, Z. Qu, S. Qiao, S. Yang, Y. Guo, P. Liu, J. Jia, Catalytic oxidation of elemental mercury over the modified catalyst Mn/γ-Al₂O₃ at lower temperatures, Environ. Sci. Technol. 44 (2010) 426–431, https://doi.org/10.1021/es9021206.

[34] D. Jampaiah, S.J. Ippolito, Y.M. Sabri, B.M. Reddy, S.K. Bhargava, Highly efficient nanosized Mn and Fe codoped ceria-based solid solutions for elemental mercury removal at low flue gas temperatures, Catal. Sci. Technol. 5 (2015) 2913–2924, https://doi.org/10.1039/c5cy00231a.

[35] L. Qiu, Y. Wang, D. Pang, F. Ouyang, C. Zhang, G. Cao, Characterization and catalytic activity of Mn-Co/TiO₂ catalysts for NO oxidation to NO₂ at low temperature, Catalysts 6 (2016) 9–18, https://doi.org/10.3390/catal6010009.

[36] X. Du, C. Li, L. Zhao, J. Zhang, L. Gao, J. Sheng, Y. Yi, J. Chen, G. Zeng, Promotional removal of HCHO from simulated flue gas over Mn-Fe oxides modified activated coke, Appl. Catal., B 232 (2018) 37–48, https://doi.org/10.1016/j.apcatb.2018.03.034.

[37] H. Pang, Z. Yang, J. Lv, W. Yan, T. Guo, Novel MnOx@Carbon hybrid nanowires with core/shell architecture as highly reversible anode materials for lithium ion batteries, Energy 69 (2014) 392–398, https://doi.org/10.1016/j.energy.2014.03.029.

[38] Z.-Y. Tian, P.H.T. Ngamou, V. Vannier, K. Kohse-Höinghaus, N. Bahlawane, Catalytic oxidation of VOCs over mixed Co–Mn oxides, Appl. Catal., B 117–118 (2012) 125–134, https://doi.org/10.1016/j.apcatb.2012.01.013.

[39] S. Todorova, H. Kolev, J.P. Holgado, G. Kadinov, Ch. Bonev, R. Pereñíguez, A. Caballero, Complete n-hexane oxidation over supported Mn–Co catalysts, Appl. Catal., B 94 (2010) 46–54, https://doi.org/10.1016/j.apcatb.2009.10.019.

[40] T. Cai, H. Huang, W. Deng, Q. Dai, W. Liu, X. Wang, Catalytic combustion of 1,2-dichlorobenzene at low temperature over Mn-modified Co₃O₄ catalysts, Appl. Catal., B 166–167 (2015) 393–405, https://doi.org/10.1016/j.apcatb.2014.10.047.

[41] S.M. Saqer, D.I. Kondarides, X.E. Verykios, Catalytic oxidation of toluene over binary mixtures of copper, manganese and cerium oxides supported on γ-Al₂O₃, Appl. Catal., B 103 (2011) 275–286, https://doi.org/10.1016/j.apcatb.2011.01.001.

[42] T. Boningari, P.R. Ettireddy, A. Somogyvari, Y. Liu, A. Vorontsov, C.A. McDonald, P.G. Smirniotis, Influence of elevated surface texture hydrated titania on Ce-doped Mn/TiO₂ catalysts for the low-temperature SCR of NOₓ under oxygen-rich conditions, J. Catal. 325 (2015) 145–155, https://doi.org/10.1016/j.jcat.2015.03.002.

[43] G. Zhang, Z. Li, H. Zheng, T. Fu, Y. Ju, Y. Wang, Influence of the surface oxygenated groups of activated carbon on preparation of a nano Cu/AC catalyst and heterogeneous catalysis in the oxidative carbonylation of methanol, Appl. Catal., B 179 (2015) 95–105, https://doi.org/10.1016/j.apcatb.2015.05.001.

[44] J.-Y. Luo, M. Meng, X. Li, X.-G. Li, Y.-Q. Zha, T.-D. Hu, Y.-N. Xie, J. Zhang, Mesoporous Co₃O₄–CeO₂ and Pd/Co₃O₄–CeO₂ catalysts: Synthesis, characterization and mechanistic study of their catalytic properties for low-temperature CO oxidation, J. Catal. 254 (2008) 310–324, https://doi.org/10.1016/j.jcat.2008.01.007.

[45] L. Li, B. Sun, J. Sun, S. Yu, C. Ge, C. Tang, L. Dong, Novel MnOₓ–CeO₂ nanosphere catalyst for low-temperature NH₃-SCR, Catal. Commun. 100 (2017) 98–102, https://doi.org/10.1016/j.catcom.2017.06.019.

[46] T. Gu, Y. Liu, X. Weng, H. Wang, Z. Wu, The enhanced performance of ceria with surface sulfation for selective catalytic reduction of NO by NH₃, Catal. Commun. 12 (2010) 310–313, https://doi.org/10.1016/j.catcom.2010.10.003.

[47] D. Fang, F. He, X. Liu, K. Qi, J. Xie, F. Li, C. Yu, Low temperature NH₃-SCR of NO over an unexpected Mn-based catalyst: promotional effect of Mg doping, Appl. Surf. Sci. 427 (2018) 45–55, https://doi.org/10.1016/j.apsusc.2017.08.088.

[48] Z. Ma, X. Wu, Z. Si, D. Weng, J. Ma, T. Xu, Impacts of niobia loading on active sites and surface acidity in NbOₓ/CeO₂–ZrO₂ NH₃–SCR catalysts, Appl. Catal., B 179 (2015) 380–394, https://doi.org/10.1016/j.apcatb.2015.05.038.

[49] L. Zhu, Y. Zeng, S. Zhang, J. Deng, Q. Zhong, Effects of synthesis methods on catalytic activities of CoOₓ–TiO₂ for low-temperature NH₃-SCR of NO, J. Environ. Sci.-China 54 (2017) 277–287, https://doi.org/10.1016/j.jes.2016.09.014.

[50] R. Moreno-Tost, J. SantamaríA-González, P. Maireles-Torres, E. Rodíguez-Castellón, A. Jiménez-López, Cobalt supported on zirconium doped mesoporous silica: a selective catalyst for reduction of NO with ammonia at low temperatures, Appl. Catal., B 38 (2002) 51–60, https://doi.org/10.1016/S0926-3373(02)00026-7.

[51] H. Li, S. Wu, L. Li, J. Wang, W. Ma, K. Shih, CuO–CeO₂/TiO₂ catalyst for simultaneous NO reduction and Hg⁰ oxidation at low temperatures, Catal. Sci. Technol. 5 (2015) 5129–5138, https://doi.org/10.1039/c5cy00794a.

[52] M.V. Gallegos, M.A. Peluso, E. Finocchio, H.J. Thomas, G. Busca, J.E. Sambeth, Removal of VOCs by catalytic process. A study of MnZnO composites synthesized from waste alkaline and Zn/C batteries, Chem. Eng. J. 313 (2017) 1099–1111, https://doi.org/10.1016/j.cej.2016.11.001.

[53] B. Zhao, H. Yi, X. Tang, Q. Li, D. Liu, F. Gao, Using CuO-MnOₓ/AC-H as catalyst for simultaneous removal of Hg⁰ and NO from coal-fired flue gas, J. Hazard. Mater. 364 (2019) 700–709, https://doi.org/10.1016/j.jhazmat.2018.04.001.

[54] B. Zhao, H.H. Yi, X.L. Tang, Q. Li, D.D. Liu, F.Y. Gao, Copper modified activated coke for mercury removal from coal-fired flue gas, Chem. Eng. J. 286 (2016) 585–593, https://doi.org/10.1016/j.cej.2015.10.107.

[55] S. Biniak, G. Szymański, J. Siedlewski, A. Świtkowski, The characterization of activated carbons with oxygen and nitrogen surface groups, Carbon 35 (1997) 1799–1810, https://doi.org/10.1016/S0008-6223(97)00096-1.

[56] Z. Tan, J. Qiu, H. Zeng, H. Liu, J. Xiang, Removal of elemental mercury by bamboo charcoal impregnated with H₂O₂, Fuel 90 (2011) 1471–1475, https://doi.org/10.1016/j.fuel.2010.12.004.

[57] Y. Huang, J. Tang, L. Gai, Y. Gong, H. Guan, R. He, H. Lyu, Different approaches for preparing a novel thiol-functionalized graphene oxide/Fe-Mn and its application for aqueous methylmercury removal, Chem. Eng. J. 319 (2017) 229–239, https://doi.org/10.1016/j.cej.2017.03.015.

[58] Y.H. Li, C.W. Lee, B.K. Gullett, Importance of activated carbon's oxygen surface functional groups on elemental mercury adsorption, Fuel 82 (2003) 451–457, https://doi.org/10.1016/S0016-2361(02)00307-1.

[59] J. Li, J. Chen, Y. Cu, C. He, Fe–Mn–Ce/ceramic powder composite catalyst for highly volatile elemental mercury removal in simulated coal-fired flue gas, J. Ind. Eng. Chem. 25 (2015) 352–358, https://doi.org/10.1016/j.jiec.2014.11.015.

[60] C. Wang, C. Zhang, W. Hua, Y. Guo, G. Lu, S. Gil, A. Giroir-Fendler, Catalytic oxidation of vinyl chloride emissions over Co-Ce composite oxide catalysts, Chem. Eng. J. 315 (2017) 392–402, https://doi.org/10.1016/j.cej.2017.01.007.

[61] H. Chen, J. Jiang, Y. Zhao, L. Zhang, D. Guo, D. Xia, One-pot synthesis of porous nickel cobalt sulphides: tuning the composition for superior pseudocapacitance, J. Mater. Chem. A 3 (2015) 428–437, https://doi.org/10.1039/c4ta04420g.

[62] B. Bai, H. Arandiyan, J. Li, Comparison of the performance for oxidation of formaldehyde on nano-Co₃O₄, 2D-Co₃O₄, and 3D-Co₃O₄ catalysts, Appl. Catal., B 142–143 (2013) 677–683, https://doi.org/10.1016/j.apcatb.2013.05.056.

[63] B. Meng, Z. Zhao, X. Wang, J. Liang, J. Qiu, Selective catalytic reduction of nitrogen oxides by ammonia over $Co_3O_4$ nanocrystals with different shapes, Appl. Catal., B 129 (2013) 491–500, https://doi.org/10.1016/j.apcatb.2012.09.040.

[64] X. Zhao, S.A. Scott, M. Huang, W. Peng, A.M. Kiefer, F.S. Flack, D.E. Savage, M.G. Lagally, Influence of surface properties on the electrical conductivity of silicon nanomembranes, Nanoscale Res. Lett. 6 (2011) 1–7, https://doi.org/10.1186/1556-276X-6-402.

[65] S. Tao, C. Li, X. Fan, G. Zeng, P. Lu, X. Zhang, Q. Wen, W. Zhao, D. Luo, C. Fan, Activated coke impregnated with cerium chloride used for elemental mercury removal from simulated flue gas, Chem. Eng. J. 210 (2012) 547–556, https://doi.org/10.1016/j.cej.2012.09.028.

[66] N.D. Hutson, B.C. Attwood, K.G. Scheckel, XAS and XPS characterization of mercury binding on brominated activated carbon, Environ. Sci. Technol. 41 (2007) 1747–1752, https://doi.org/10.1021/es062121q.

[67] H. Li, S. Wu, C.-Y. Wu, J. Wang, L. Li, K. Shih, SCR atmosphere induced reduction of oxidized mercury over $CuO-CeO_2/TiO_2$ catalyst, Environ. Sci. Technol. 49 (2015) 7373–7379, https://doi.org/10.1021/acs.est.5b01104.

[68] W. Xu, H. He, Y. Yu, Deactivation of a $Ce/TiO_2$ catalyst by $SO_2$ in the selective catalytic reduction of NO by $NH_3$, J. Chem. Phys. C 113 (2009) 4426–4432, https://doi.org/10.1021/jp8088148.

[69] G. Qi, R.T. Yang, R. Chang, $MnO_x$-$CeO_2$ mixed oxides prepared by co-precipitation for selective catalytic reduction of NO with $NH_3$ at low temperatures, Appl. Catal., B 51 (2004) 93–106, https://doi.org/10.1016/j.apcatb.2004.01.023.

[70] C. Yu, B. Huang, L. Dong, F. Chen, Y. Yang, Y. Fan, Y. Yang, X. Liu, X. Wang, Effect of Pr/Ce addition on the catalytic performance and $SO_2$ resistance of highly dispersed $MnO_x$/SAPO-34 catalyst for $NH_3$-SCR at low temperature, Chem. Eng. J. 316 (2017) 1059–1068, https://doi.org/10.1016/j.cej.2017.02.024.

[71] C. Sun, H. Liu, W. Chen, D. Chen, S. Yu, A. Liu, L. Dong, S. Feng, Insights into the Sm/Zr co-doping effects on $N_2$ selectivity and $SO_2$ resistance of a $MnO_x$-$TiO_2$ catalyst for the $NH_3$-SCR reaction, Chem. Eng. J. 347 (2018) 27–40, https://doi.org/10.1016/j.cej.2018.04.029.

[72] Z. Wu, R. Jin, H. Wang, Y. Liu, Effect of ceria doping on $SO_2$ resistance of $Mn/TiO_2$ for selective catalytic reduction of NO with $NH_3$ at low temperature, Catal. Commun. 10 (2009) 935–939, https://doi.org/10.1016/j.catcom.2008.12.032.

[73] H. Jiang, Y. Niu, Q. Wang, Y. Chen, M. Zhang, Single-phase $SO_2$-resistant to poisoning Co/Mn-MOF-74 catalysts for $NH_3$-SCR, Catal. Commun. 113 (2018) 46–50, https://doi.org/10.1016/j.catcom.2018.05.017.

[74] Y. Huang, D. Gao, Z. Tong, J. Zhang, H. Luo, Oxidation of NO over cobalt oxide supported on mesoporous silica, J. Nat. Gas Chem. 18 (2009) 421–428, https://doi.org/10.1016/s1003-9953(08)60135-8.

[75] H. Zeng, F. Jin, J. Guo, Removal of elemental mercury from coal combustion flue gas by chloride-impregnated activated carbon, Fuel 83 (2004) 143–146, https://doi.org/10.1016/S0016-2361(03)00235-7.

[76] H. Li, C.-Y. Wu, Y. Li, J. Zhang, $CeO_2$-$TiO_2$ catalysts for catalytic oxidation of elemental mercury in low-rank coal combustion flue gas, Environ. Sci. Technol. 45 (2011) 7394–7400, https://doi.org/10.1021/es2007808.

[77] P. Lu, C. Li, G. Zeng, L. He, D. Peng, H.C. Li, Y. Zhai, Low temperature selective catalytic reduction of NO by activated carbon fiber loading lanthanum oxide and ceria, Appl. Catal., B 96 (2010) 157–161, https://doi.org/10.1016/j.apcatb.2010.02.014.

[78] M. Casapu, O. Kröcher, M. Elsener, Screening of doped $MnO_x$–$CeO_2$ catalysts for low-temperature NO-SCR, Appl. Catal., B 88 (2009) 413–419, https://doi.org/10.1016/j.apcatb.2008.10.014.

[79] Y. Li, P.D. Murphy, C. Wu, K. Powers, J.C.J. Bonzongo, Development of silica/vanadia/titania catalysts for removal of elemental mercury from coal combustion flue gas, Environ. Sci. Technol. 42 (2008) 5304–5309, https://doi.org/10.1021/es8000272.

[80] S. Niksa, N. Fujiwara, A predictive mechanism for mercury oxidation on selective catalytic reduction catalysts under coal-derived flue gas, J. Air Waste Manage. 55 (2005) 1866–1875, https://doi.org/10.1080/10473289.2005.10464779.

[81] C. He, B. Shen, F. Li, Effects of flue gas components on removal of elemental mercury over Ce-$MnO_x$/Ti-PILCs, J. Hazard. Mater. 304 (2016) 10–17, https://doi.org/10.1016/j.jhazmat.2015.10.044.

[82] G. Marbán, T. Valdés-Solís, A.B. Fuertes, Mechanism of low-temperature selective catalytic reduction of NO with $NH_3$ over carbon-supported $Mn_3O_4$ Role of surface $NH_3$ species: SCR mechanism, J. Catal. 226 (2004) 138–155, https://doi.org/10.1016/j.jcat.2004.05.022.

[83] M. Kang, E.D. Park, J.M. Kim, J.E. Yie, Cu–Mn mixed oxides for low temperature NO reduction with $NH_3$, Catal. Today 111 (2006) 236–241, https://doi.org/10.1016/j.cattod.2005.10.032.

[84] A.A. Presto, E.J. Granite, Survey of catalysts for oxidation of mercury in flue gas, Environ. Sci. Technol. 40 (2006) 5601–5609, https://doi.org/10.1021/es060504i.

[85] R. Grabowski, S. Pietrzyk, J. Słoczyński, F. Genser, K. Wcisło, B. Grzybowska-Świerkosz, Kinetics of the propane oxidative dehydrogenation on vanadia/titania catalysts from steady-state and transient experiments, Appl. Catal., A 232 (2002) 277–288, https://doi.org/10.1016/S0926-860X(02)00117-5.